الجمهورية الجزائرية الديمقراطية الشعبية
PEOPLE'S DEMOCRATIC REPUBLIC OF ALGERIA
وزارة التعليم العالي والبحث العلمي
MINISTRY OF HIGHER EDUCATION AND SCIENTIFIC RESEARCH
جامعة سعد دحلب البليدة1
UNIVERSITY OF SAAD DAHLEB BLIDA 1

كلية العلوم
Faculty of Sciences
دائرة الفيزياء
Department of Physics

MASTER DIPLOMA THESIS
In Physics
Option: Nanophysics

THEME

SYNTHESIS OF NANOSTRUCTURED LAYERS OF DOPED IRON DISULFIDE (FeS_2) FOR A PHOTOVOLTAIC APPLICATION

Presented by:

Ms. Karima NADJI

Ms. Mahdjouba BENSEHIL

Defensed on 14/10/2020 in front of the jury composed of:

Dr. Y. Berbar	MCA	USTHB	President
Dr. N. Ouarab	MRB	CRTSE	Supervisor
Dr. A. Hassein-Bey	MCB	USDB	Co-Supervisor
Dr. W. Laslouni	MCB	USDB	Examiner

Blida 1-2019/2020

Acknowledgments

Praise is to Allah for allowing us to complete this research work, carried out within Semiconductor Technology Research Center for Energetics (CRTSE).

First of all, we thank Almighty Allah for giving us the strength, will, and privilege to study and follow the path of science.

We would like to express our sincere thanks to the thesis Director, ***Dr. Nouredine OUARAB****, Senior Researcher at CRTSE, for the help, support, advice, and guidance he has provided to us during these months, which we reiterate our deep gratitude.*

We would also like to thank our co-supervisor of thesis ***Dr. Abdelkader HASSEIN-BEY****, Senior Lecturer at the Saad Dahlab University of Blida-1, for the help of accomplishment of our work, for the scientific and technical training he provided to us, his advice and encouragement.*

We hold to warmly thank ***Dr. Yassine BERBAR****, Senior Lecturer at University Of Science And Technology Houari Boumediene, to have accepted to chair the jury of this thesis.*

We hold to present our thanks to ***Dr. Warda LASLOUNI****, Senior Lecturer at the Saad Dahlab University of Blida-1, for her willingness to evaluate this thesis.*

We hold highly to express our deep recognition and our gratitude to all professors of the physics department at the Saad Dahlab University, for all they have given us.

We gratefully acknowledge to our families who always encouraged us to pursue our scientific way to this distant point and supporting us spiritually throughout this thesis as well as throughout our life so far in all its manifestations.

Last but not least, we would like to thanks to all our colleagues at the Saad Dahlab University of Blida-1, all our friends and all the people who encouraged us during these years.

Dedications

I dedicate this work to:

My very dear parents

For their sacrifices and their efforts

My sister Amina

My brothers Amine and Aymane,

The whole family

And Mr. Tahar BOUDELLA for his support and his encourage

My partner in this research work

My friends

To everyone I love

KARIMA

Dedications

I dedicate this work to:

My parents

My brothers

My partner in this work

All my friends

MAHDJOUBA

Abstract

Iron disulfide has attracted a lot of interest in the field of photovoltaic applications due to its favorable electronic and optical properties. This work focuses on the elaboration of nanostructured FeS_2 thin films for photovoltaic solar cell applications. By using the simplest and least expensive deposition processes, the method leads to the synthesis of iron disulfide thin films with the desirable pyrite phase. Therefore, the emphasis is placing on the chemical bath deposition (CBD) method. The study of iron disulfide thin films requires the use of many characterization techniques for structural, morphological, electrical and optical analysis.

Keywords: iron disulfide, pyrite, thin films, photovoltaic, chemical bath deposition

ملخص

اجتذب ثاني كبريتيد الحديد الكثير من الاهتمام في مجال التطبيقات الكهروضوئية نظرًا لخصائصه الإلكترونية والبصرية الملائمة. يركز هذا العمل على تطوير أغشية FeS_2 الرقيقة ذات البنية النانوية لتطبيقات الخلايا الشمسية الكهروضوئية، باستخدام أبسط عمليات الترسيب وأقلها تكلفة، والتي تؤدي إلى تخليق أغشية رقيقة من ثاني كبريتيد الحديد مع طور البيريت المرغوب فيه. لذلك، سيتم التركيز طريقة ترسيب الحمام الكيميائي (CBD). تتطلب دراسة الأغشية الرقيقة لثاني كبريتيد الحديد استخدام العديد من تقنيات التوصيف للتحليل الهيكلي والمورفولوجي للأغشية التي تم الحصول عليها.

كلمات مفتاحية: ثاني كبريتيد الحديد، البيريت، الأغشية الرقيقة، الكهروضوئية، ترسيب الحمام الكيميائي

Résumé

Le disulfure de fer a suscité beaucoup d'intérêt dans le domaine des applications photovoltaïques en raison de ses propriétés électroniques et optiques favorables. Ce travail se concentre sur l'élaboration de couches minces nanostructurées de FeS_2 pour des applications de cellules solaires photovoltaïques. En utilisant les procédés de dépôt les plus simples et les moins coûteux, le procédé conduit à la synthèse de films minces de disulfure de fer avec la phase de pyrite souhaitable. Par conséquent, l'accent est mis sur la méthode de dépôt par bain chimique (CBD). L'étude des couches minces de disulfure de fer nécessite l'utilisation de nombreuses techniques de caractérisation pour l'analyse structurelle, morphologique, électrique et optique.

Mots clés : disulfure de fer, couches minces, photovoltaïque, dépôt par bain chimique

Contents

Acknowledgments i
Dedications ii
Abstract iv
Contents v
Nomenclature vii
List of figures viii
List of tables x
Introduction 01
Chapter I : Generalities on Iron Disulfide Properties and Applications
I.1 Introduction 03
I.2 Definition 03
I.3 Iron disulfide properties 04
I.3.1 Electronic properties 04
I.3.2 Optical properties 05
I.3.3 Electrical properties 09
I.3.4 Elastic properties 11
I.4 Iron disulfide applications 11
I.5 Thin film 12
I.5.1 Definition 12
I.5.2 Thin film formation mechanism 12
I.5.3 Deposition of iron disulfide thin film mechanism 13
I.5.4 Nanostructuration of iron disulfide thin layers 15
Chapter II : Synthesis methods of FeS_2 nanostructures
II.1 Introduction 18
II.2 Deposit techniques 18
II.2.1 Chemical Vapor Deposition (CVD) 19
II.2.2 Chemical Bath Deposition (CBD) 22
II.2.2.1 Solution chemistry 22
II.2.2.2 Substrate effects 25
II.2.2.3 Process control 27
II.2.2.4 CBD advantages and limitations 28
Chapter III : FeS_2 Characterization Techniques
III.1 Introduction 29

III.2 X-ray Diffraction (XRD) 29
III.3 Field Emission Scanning Electron Microscopy (FE-SEM) 31
III.4 Raman spectroscopy 32
III.5 Ultraviolet–visible spectroscopy 34
III.6 Profilometer 36
III.7 FTIR spectroscopy. 36
III.8 Film lifetime measurement. 37
Chapter IV : Results and discussion
IV.1 Experimental details and films preparation. 39
IV.2 Structural and morphology characterizations. 39
IV.2.1 X-ray diffraction 39
IV.2.2 Raman spectroscopy 41
IV.2.3 SEM micrographs analysis 42
IV.3 FTIR spectroscopy and composition identification. 44
IV.4 Diffuse reflectance measurements. 45
IV.5 Lifetime results. 47
Conclusion 50
References 51

Nomenclature

Frequently used abbreviations:

APCVD	Atmospheric Pressure Chemical Vapor Deposition
BSEs	Backscattered Electrons
CBD	Chemical Bath Deposition
CMOS	Complementary Metal Oxide Semiconductor
CVD	Chemical Vapor Deposition
EMR	Electromagnetic Radiations
eV	Electron Volts
FE-SEM	Field Emission Scanning Electron Microscopy
FTIR	Fourier Transform Infrared Spectroscopy
HPCVD	Hybrid Physical–Chemical Vapor Deposition
LA	Longitudinal Acoustic
LPCVD	Low Pressure Chemical Vapor Deposition
LP-MOCVD	Low-Pressure Metal-Organic Chemical Vapor Deposition
LVDT	Linear Variable Differential Transformer
MOCVD	Metal Organic Chemical Vapor Deposition
PEs	Primary Electrons
SAMs	Self-Assembled Monolayers
SEM	Scanning Electron Microscopy
SEs	Secondary Electrons
SILAR	Successive Ionic Layer Adsorption and Reaction
TA	Transversal Acoustic
TMDs	Transition Metal Disulfides
UHVCVD	Ultra High Vacuum Chemical Vapor Deposition
UV	Ultraviolet
VIS	Visible
XRD	X-ray Diffraction

List of figures

I.1	Crystal structures of FeS_2 (a) Pyrite and (b) marcasite, Yellow (blue) spheres represent S (Fe) atoms.	04
I.2	(a) the electronic band structures of iron pyrite investigated after crystalline relaxation. (b) The diagram of the energy levels, in the case of Ni-doping, of given by ab-initio calculation (Fe–Ni)-3d and S-3p orbitals presented by blue and red color, respectively.	05
I.3	Total density of states of pure pyrite iron disulfide is measured by LDA-TB-mBJ method.	05
I.4	Absorption coefficients $\alpha(\omega)$ are calculated as function of photon energy range extended to 8 eV of pure iron pyrite, left spectrum. The reflectivity behavior of the materials is shown in the right.	06
I.5	Three modes of thin film growth processes.	13
I.6	Schematic illustration of the spray device.	13
I.7	Schematic diagram of a chemical vapor deposition (CVD) system.	14
I.8	Schematic illustration of the chemical bath device.	14
I.9	Schematic illustration of the formation of FeS_2 thin films.	15
I.10	SEM images of the FeS_2 nanoparticles by sol–gel method (a) in ref (74). and (b) in ref (91).	16
I.11	SEM images of various 1D FeS_2 nanostructures by controlling iron sources, the molar concentration of precursors and reaction temperature.	16
I.12	SEM images for (a) FeS_2 nanoplates and (b) FeS_2 nanosheets.	17
I.13	SEM images of the FeS_2 microspherolites by microwave irradiation (a) low magnification and (b) high magnification.	17
II.1	The principle of CVD.	20
II.2	Important reaction zones in CVD.	20
II.3	Precursor transport and reaction processes in CVD.	21
II.4	Schematic illustration of the effect of solution pH and metal concentration [M] on the tendency of a solution to resolve a solid phase.	23
II.5	Mechanisms for the formation of inorganic films from aqueous inorganic solutions.	25
II.6	Schematic illustration of the effect of the zeta potentials ($\zeta 1$ and $\zeta 2$) of two adjacent surfaces on the nature of the electrostatic interaction between them.	26

III.1	Geometrical condition for diffraction from lattice planes.	30
III.2	Diffractometer D8 Advance Brucker (CDTA).	30
III.3	Main signals emitted as a result of the interaction between the electron beam and the sample.	31
III.4	Field emission scanning electron microscope (CRTSE).	32
III.5	Rayleigh and Raman scattering.	33
III.6	Raman spectroscopy (CDTA).	34
III.7	Spectrophotometer (CRTSE).	35
III.8	Schematic diagram of the spectrophotometer.	35
III.9	Schematic view of the FTIR spectrophotometer	37
III.10	Schematic diagram of the FTIR spectrophotometer.	37
III.11	Schematics of the Sinton WCT-120 series QSSPC instrument.	38
III.12	The WCT-120PL is an affordable, tabletop silicon lifetime and wafer metrology system.	38
IV.1	X-ray diffraction patterns coming from three-samples corresponding to the time deposition variation.	40
IV.2	Raman spectra in the 50–1200 cm-1 wavenumber range of the three samples.	42
IV.3	SEM micrographs of the samples: 60 min (a1; a2), 90 min (b1; b2), and 120 min (c1; c2).	43
IV.4	Fourier-transform infrared (FTIR) spectra of the three samples as indicated in figure corresponding to the time deposition variation	45
IV.5	Reflectance diffuse	46
IV.6	Measurements of lifetimes of thin layer of iron disulfide	48

List of tables

I.1	Reported optical properties of FeS2 materials with different structures.	08
I.2	below shows the different properties of iron disulfide	08
I.3	Reported electrical properties of FeS2, materials prepared by different technologies.	10
IV.1	Details of measured lifetime in these experiments	48

Introduction

Introduction

The performance of photovoltaic solar cells is closely linked to the properties of materials from which they are made. Or, many problems are linked to these materials have arisen concerning the increasing of the coefficient of efficiency and the development of less expensive and non-toxic solar cells. So, nanostructured metal disulfides show great potential for the development of various novel and smart devices, including photovoltaic solar cells. These metal sulfides have been widely studied because of their unique electrical, optical, chemical and magnetic properties [1, 2].

Iron disulfide (FeS_2), one of the transition-metal sulfides, has the most elemental storage in the earth. FeS_2 has two common crystal structures; cubic-system pyrite and orthorhombic-system marcasite. Iron disulfide has attracted a lot of interest in photovoltaic and photo-electrochemical applications due to its favorable electronic and optical properties. In recent decades, FeS_2 has drawn considerable attention from both industrial and academic communities as a competitive candidate working material for efficient and inexpensive solar energy conversion, mainly because of its suitable bandgap, extraordinary absorption coefficient, nontoxicity, and low cost of raw materials [3].

So, materials elaboration at nano-scale dimensions is overseeing by the term of quantum confinement, for which it exhibits specific physical properties that do not exist either in bulk or surface states. Nanocrystals, nanowires, and nanotubes of FeS_2 were synthesizing by physical methods, such as thermal evaporation and DC magnetron sputtering, likewise by chemicals, such as chemical bath deposition, electroplating, sol-gel, dip coating, and spin coating. Most of these techniques have been motivated by efficient synthetic routes to control morphology, stability, and shape dispersion. Many common methods, including hydrothermal, hot injection, solvothermal, and sulfidation, have also been used for the preparation of high-quality FeS_2 nanostructures. Despite this, the conversion efficiency of pyrite (FeS_2) based solar cells has remained low, which has been attributed to phase impurity. In other words, FeS_2 can be crystallized not only into a cubic pyrite structure but also into an orthorhombic metastable marcasite structure, which is detrimental to photovoltaic applications due to its low bandgap. New and improved techniques are therefore needed to solve these problems. Besides, simple methods for the preparation of large-area polycrystalline pyrite thin films using low-cost equipment should also be developed [4, 5].

Historically, the name of pyrite structure comes from the Greek around 50 AD. Pyrite was noticed by the ancients for the sparks it produces under shocks and it is used to produce fire. It was not until the beginning of the 20th century that it was studied scientifically and it was one of earliest structures to be determined by X-ray diffraction, where works of Bragg, Ewald and Friedrich were dependent on the use of single crystals, as it was recommended by the Laue's method [6]. Given these properties, many scientists have interest for its use (in the 1980s) for the realization of thin-film solar cells. However, it lost its usefulness in the 1990s, when energy conversion efficiencies never exceeded 2.8%, which is a disappointing result [7]. This boring performance is widely recognized as being due to some fundamental problems related to the appears of the marcasite phase (band gap of 0.34 eV), intrinsic surface states (gap states) and defects such as bulk sulfur vacancies of the pyrite that have not been resolved for almost three decades [8].

The ongoing work aims to provide insight into the formation mechanism of nano-particles and to highlight its compatibility with the elaboration process. The demonstration of the structural behavior made thorough many characterization techniques, which have been adopted using, for this issue, glancing incidence X-ray diffraction (GIXRD) 2θ scans, Raman spectroscopy, field effect scanning electron microscopy (FE-SEM), and Fourier transform infrared (FTIR). Also for electronic and optical properties, the QSSPC and the UV-Vis-IR spectrophotometer are used.

The present memory is presented through four chapters. So in the first chapter, we expose the generalities about the properties and applications of iron disulfide. After that, we will outline the thin films growth mechanisms and discuss the deposition methods available for synthesis the pyrite thin films. The chapter 2 is dedicated to the description of the most suitable methods for the deposition of pyrite thin films, which will be tried in this study. The third chapter is devoted to the explanation of the different characterization and analysis techniques used for the study of the physicochemical and optical characteristics of thin films. The last chapter is dedicated to analysis and discussion.

Chapter I

Generalities on Iron Disulfide Properties and Applications

I. Generalities on Iron Disulfide

This chapter is devoted to a general description of iron disulfide. In the first part, we will present its properties and applications. Then, we will end this chapter by describing the growth mechanisms of thin films.

I.1. Introduction

Pyrite iron disulfide (FeS_2) is a typical representative and a popular topic among the research on metal sulfide due to most importantly, the advantages of earth-abundance, nontoxicity, and low cost [9]. Since pyrite FeS_2 was first explored as a photovoltaic semiconductor in 1983, there has been continuous interest in that material novelty. It was employed as high-performance electrode material in rechargeable batteries [10, 11]. With the development of new technologies and the increasing demands for energy, more and more efforts have been dedicated to the exploitation of advanced anode materials for power storage device [12, 13]. It can be used as a dilute magnetic semiconductor for spintronics [14], photo-catalysis [15], photo-capacitors [16], hydrogen production, and photo-electrochemical cells [17]. These materials have the chemical formula TMS_2 (TM = Sc, Ti, V, Cr, etc.) from which the iron disulfide (FeS_2) is derived [18]. Iron disulfide came into attention primarily in the 1980s after the oil crisis, which acted as a catalyst in driving research activities towards finding an ideal solar absorber material [19, 20] due to its very high optical absorption coefficient over a wide range of frequencies and its suitable bandgap [5, 19]. In the addition of the thin film surface state, synthesis of nanostructured layers of iron disulfide is a very active field as attested by the literature [21] in which it shows great potential for the development of various novel and smart devices [1].

I.2. Definition

FeS_2 has two common crystal structures; cubic-system pyrite and orthorhombic-system marcasite. Iron marcasite (m-FeS_2) is the polymorph of pyrite FeS_2, which fundamentally different from each other. The structure of p-FeS_2 belongs to space group Pa-3 in the cubic crystal system, while m-FeS_2 possesses an orthorhombic crystal system in space group Pnnm. Nevertheless, m-FeS_2 always be considered as a non-convenient impurity of p-FeS_2, in photovoltaic materials due to its reported narrow bandgap (0.34 eV) [22]. Fig I.1 (a) and (b) show the schematic view of pyrite and marcasite structures of FeS_2. The lattice parameters of pyrite (cubic β-FeS_2, "fool's gold") are a = b = c = 0.541 nm, the bond length of Fe-S and S-S are 0.23 nm and 0.21 nm, respectively. The structure of cubic FeS_2 is similar to

that of NaCl. Namely, Fe^{2+} and S_2^{-2} displace the lattice sites of Na^+ and Cl^-, respectively. One iron atom is surrounded by six nearest neighbor S atoms, towards six of the eight faces of a distorted octahedron, and one sulfur atom is surrounding by three Fe atoms forming tetrahedral coordinates [4]. The positions of *X* ions in the pyrite structure may be derived from the fluorite structure, starting from a hypothetical $Fe^{2+}(S^-)_2$ structure. The S^- ions in FeS_2 are shifted from these high symmetry positions along <111> axes to reside on Wyckoff parameters (*uuu*) and symmetry-equivalent positions. Here, the parameter *u* should be regarded as a free atomic parameter that takes different values in different pyrite-structure compounds (iron pyrite FeS_2: *u*(S) = 0.385). The shift from fluorite *u* = 0.25 to pyrite *u* = 0.385 is rather large and creates an S–S distance that is clearly a binding one.

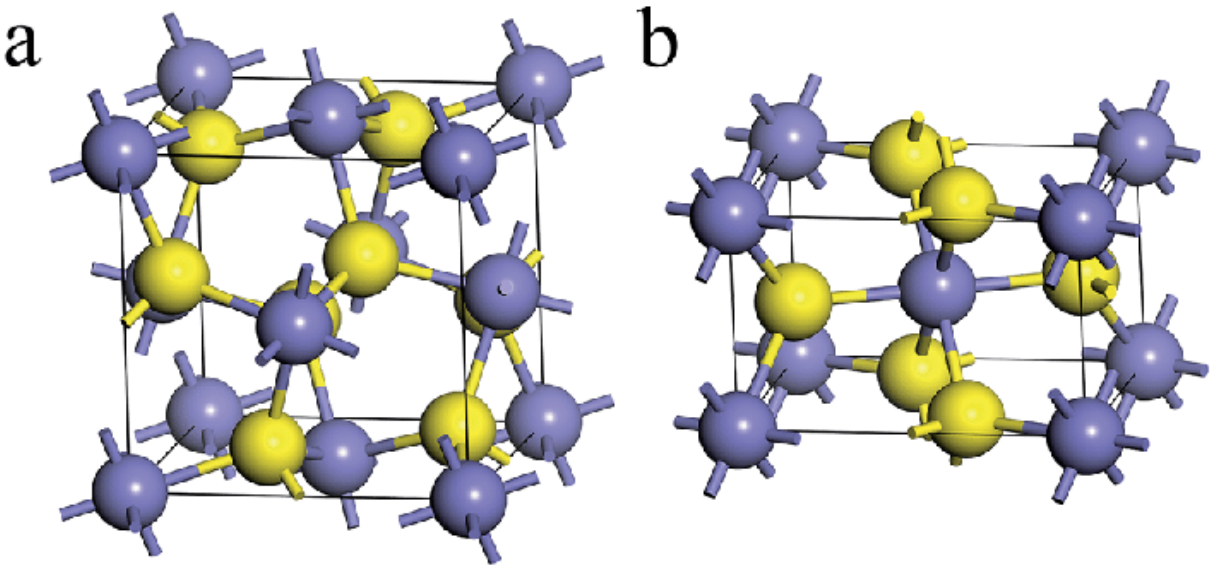

Figure I.1. *Crystal structures of FeS_2 (a) Pyrite and (b) marcasite, Yellow (blue) spheres represent S (Fe) atoms* [3].

I.3. Iron disulfide properties

I.3.1. Electronic properties

As we know, FeS_2 is an indirect bandgap semiconductor of 0.95 eV, as exposed in Fig. I.2, the maximum and minimum of the valence (VBM) and the conduction bands (CBM) are locating at the X and Γ-high symmetry points, respectively [23– 25]. So, these valence and conduction bands have formed by the splitting of the 3d orbitals of Fe atom into two groups, known as t_{2g} and eg. The unoccupied states in conduction bands are mixtures of Fe_{eg} and $S_{pp\sigma*}$ states, which is crucial for efficient optical absorption. Likewise, the band structure of pure pyrite shows a critical transition of approximately 1.8 eV sited along X-M, suitable for the PV industry. This transition results between Fe_{t2g} state and the mixed Fe–S state (Fe_{eg} + $S_{pp\sigma*}$) at

the X high-symmetry point. The bandgap in FeS_2 has been pointed out in various experimental and theoretical works [25–28] that it can be affected by structural changes.

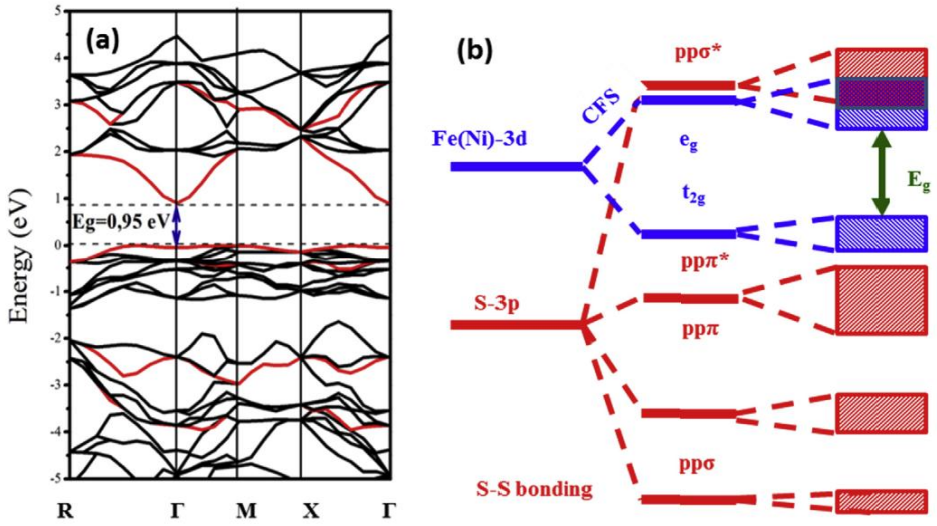

Figure. I.2. *(a) the electronic band structures of iron pyrite investigated after crystalline relaxation given by ab-initio calculation [29]. (b) The diagram of the energy levels, in the case of Ni-doping, of (Fe–Ni)-3d and S-3p orbitals presented by blue and red color, respectively.*

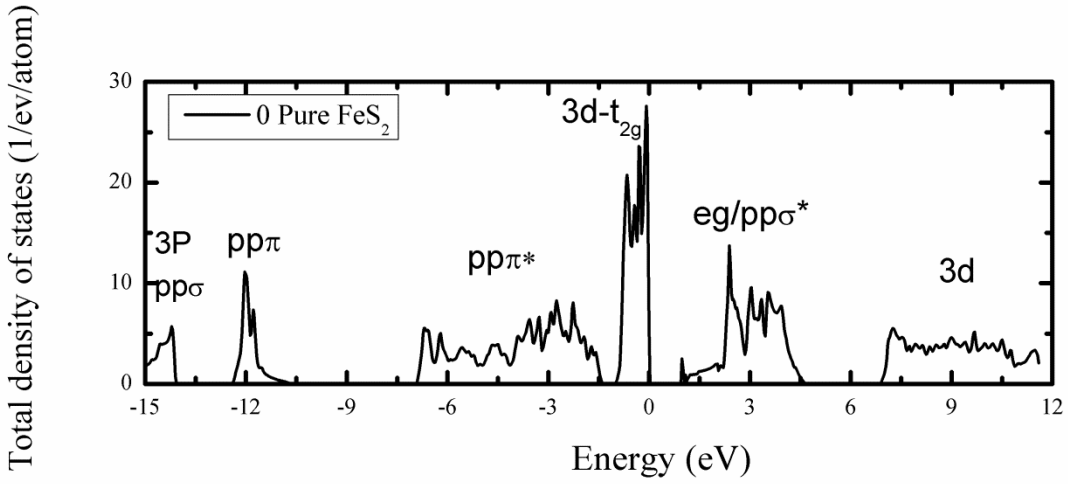

Figure. I.3. *Total density of states of pure pyrite iron disulfide is measured by LDA-TB-mBJ method.*

I.3.2. Optical properties

The study of optical properties has driven an essential part of this work. However, the production of high-quality pyrite thin films and nanocrystals has been reported [30–32] as a solution to enhance the low open-circuit voltage. So, we expose the fundamental question about optical absorption associated with the increase of the optical gap. In this matter, figures.I.4 give the response of FeS_2 to the light, which produces optical transitions between occupied and unoccupied states. For 3d metals, it is appropriate to include the intraband contributions to the optical conductivity tensor basing on the phenomenological Drude model [33] with intraband Drude relaxation time γ_D=0.6 eV. Within the electric dipole hypothesis,

optical absorption spectra mostly resulted from transitions between 3d-t2g states to mixtures of 3deg and S-$S_{pp\sigma^*}$ states [34]. In the following, the threshold of the optical response occurs at energy of 0.98 eV, which denotes the bandgap of pure iron pyrite between Γ-X high symmetry points. In edict to observe the absorption coefficients $\alpha\ (\omega)$ and the reflectivity $R(\omega)$ of FeS_2 as depicted in figures I.4, we have analyzed the main electronic contributions to the appeared peaks by partitioning the optical absorption coming from transitions between $3d_{t2g} \rightarrow 3d_{eg}$, S-$3p_{pp\pi^*} \rightarrow$ S-$3p_{pp\sigma^*}$, S- $3p_{pp\pi^*} \rightarrow 3d_{eg}$ and $3d_{t2g} \rightarrow$ S-$3p_{pp\sigma^*}$. At an energy range of [1.45–6] eV, the absorption coefficient increases linearly until it reaches the value of ($16*10^5$) cm^{-1} within an optical gap of 1.45eV. Similarly, the reflectivity spectra show the reaction of this compound to the incident light, and the intensity is between 30% and 48% forming curious peaks due to the same transitions.

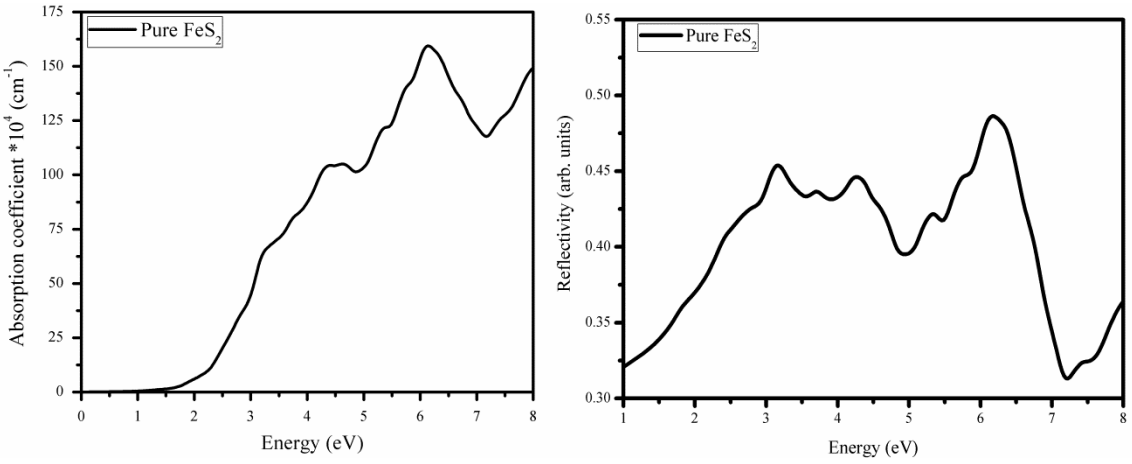

Figure. I.4. *Absorption coefficients α(ω) are calculated as function of photon energy range extended to 8 eV of pure iron pyrite, left spectrum. The reflectivity behavior of the materials is shown in the right.*

In the experimental situation, parameters that were used to characterize the optical properties of semiconductors include optical absorption coefficient α(ω), energy bandgap (E), extinction coefficient, and refractive index. The absorption coefficient and the energy bandgap are the two most popular parameters, which are widely studied and applied. They can be calculated according to the optical spectra tested with an ultraviolet-visible spectrophotometer. The absorption coefficient α(ω) is obtained by the following equation [35]:

$$\alpha(w) = \frac{2.303\mathrm{Log}\left(\frac{I_0}{\mathrm{I}}\right)}{d} + \frac{Ln(1-R)}{d} \quad and \ Absorbance\ (Abs) = Log\left(\frac{I_0}{\mathrm{I}}\right) \qquad (\mathrm{I}.1)$$

Where I_0 is the incident intensity; I is the transmitted light intensity; d is the thickness of the sample; R represents the reflectivity; Abs represents the absorbance. The value of $\alpha(w)$ can be obtained using the measured Abs value from the light absorption spectrum and d value from SEM or other approaches. Semiconductors can be divided into two types: direct and indirect bandgap semiconductors. It can be distinguished by the feature of the shoulder structure shown in the liner absorption area. The indirect bandgap semiconductor has a shoulder structure while the direct type has no shoulder structure. The variation may be caused by the different energy band structures. Similarly, the energy bandgap can also be fitted with the linear absorption area in the optical absorption spectrum. The Eg value can be calculated by conventional Tauc equation [36] :

The Eg value can be calculated by conventional Tauc equation [36] :

$$\alpha(w) = A(hv - E_g)^n \quad (\text{I}.2)$$

Where hv represents the energy of the incident photon, and A represents a constant. n = 2 for an indirect bandgap semiconductor and n = 1/2 for a direct bandgap semiconductor. The E, value is obtained by fitting the absorption coefficient to the general formula.

A large number of researches discover a common phenomenon that pyrite FeS_2 shows an optical absorption coefficient (10^6 cm^{-1}). Energy bandgap has a close relationship with the preparation methods, morphology, and structure of materials. Takabashi et al. [37] prepared FeS_2 films by CVD method under normal pressure. The films showed an absorption coefficient of 5.10^5 cm^{-1} when the photon energy was larger than 2 eV. They found that the absorption coefficient value changed with the change in the ratio of chemical ingredients. Meng et al. [38] prepared various FeS_2 films by sulfidation of magnetron sputtered Fe films under different sulfur pressure and tested their optical absorption performance. The absorption coefficient is distributed in the range of $(4\text{-}8).10^5$ cm^{-1}. Recently, they fabricated one-dimensional FeS_2 nanoarray films by the template-directed synthesis in the combination of subsequent sulfidation. The FeS_2 nanoarray films exhibited excellent light absorption with an absorption coefficient 2.10^5 cm^{-1} and an energy bandgap of 0.89 eV. Sanchez et al. [39] systematically studied the relationship between the absorption edge of FeS_2 films and the testing temperature, so the optical absorption coefficient increased exponentially with the increase of photon energy; when it was at 100-300 K. Impurity was considered to be detrimental to the electron and photonic performance of photoelectrodes. In contrast to the traditional view that marcasite was a deleterious phase in FeS_2, a recent report suggested that marcasite was beneficial for the charge separation across the pyrite-marcasite phase junction [40]. Results indicate that the optical properties of FeS_2, films are closely related to the

microstructure, synthesis approach, and defects. Table. I.1 summarizes the reported optical properties of FeS_2 materials prepared by different methods and with different structures.

Table I.1. Reported optical properties of FeS2 materials with different structures.

Structure	Preparation method	$\alpha(w)$ cm^{-1}	E_g (eV)	Reference
Nanoparticles	CVD	0.5×10^5	0.95	[41]
Nanoparticles	Spray pyrolysis	0.5×10^5	0.72	[42]
Nanoparticles	Spray pyrolysis	0.5×10^5	0.73	[43]
Nanoparticles	Magnetron sputtering	1.2×10^5	0.8-1.6	[44]
Nanoparticles	Magnetron sputtering	0.5×10^5	0.8-1.3	[45]
Nanoparticles	Sol-gel	3×10^5	0.9-0.99	[46]
Cubes octahedral	Hydrothermal	0.26×10^5	1.25	[47]
Nanocrystals	Hot inhection	_	0.88-0.91	[48]
Nanocrystals	Hot inhection	2×10^5	0.93	[49]
Nanowires	Direct sulfidation	_	0.89	[20]
Nanocubes	Chemical bath deposition	~10^6	~1.1	[50]
Nanorods	Sulfidation of percursors	1.2×10^5	0.89	[51]
Nanotubes		1.8×10^5	0.77	[52]

Table I.2. below shows the different properties of iron disulfide [20, 53, 54].

Properties	**Values**
Band gap	0.95 eV (indirect)
Mobility	>300 $cm^2.v^{-1}.s^{-1}$ (in single crystal form)
Minority carrier diffusion length	100-1000 nm
Absorption	$\alpha = 6\times10^5$ cm^{-1} for $h\nu > 1.3$ eV
Density	4.7-4.87 g/cm3
Decomposition Temperature	600°C
Heat of Vaporization	18.67 kJ/mol
Melting Point	1194°C
Mohs Hardness	6.3
Refractive Index	1.56
Solubility in H_2O	negligible (insoluble)
Molecular Weight	119.98
Toxicity	non-toxic
Appearance	dark gray to black metallic solid

I.3.3. Electrical properties

The conventional conducting mechanism, namely, electron transition between the conduction band and valence band, is not suitable to explain the conductivity change of FeS_2 films. Ares et al, [55] proposed a model of grain boundary electron barrier, which considered the effects of temperature and grain boundary on the conductivity behavior. Based on the model, Baccarnai et al.[56] further modified it and proposed an improved version to allow the description of polycrystalline semiconductor materials. There are several grain boundaries and defects (broken bonds, vacancies, and dislocations) existed in the inner of polycrystalline materials, leading to the production of defect level in the region close to the bottom of the conduction band. Carriers are prone to be captured when crossing grain boundaries, and the barrier would produce at a grain boundary, which would affect the electrical properties of films. The resistivity and temperature satisfy the following equation:

$$\rho = \frac{A'}{T^n} exp^{(\frac{q\phi_B}{KT})} \quad (I.3)$$

Where A' is a constant, T^n is thermodynamic temperature, q is unit charge, k is Boltzmann constant and ϕ_B is the barrier height of grain boundary. The equation is suitable for describing the conducting behavior at high temperature. Efros et al.[57] made some corrections and proposed a suitable mechanism which follows the relationship expression:

$$\rho = BTexp^{(\frac{T_E}{T})^{1/2}} \quad (I.4)$$

For single-crystalline semiconductor materials, the grain boundary barrier model based on boundary theory is obviously not suitable for this system. Ares et al. [55] have proposed the point defect model in which the electrical behavior of FeS_2 is dominated by the point defects that occurred in the crystal. The relationship between resistivity and temperature are expressing by the equation:

$$\rho = \rho_0 exp^{[\frac{E_m}{K}(\frac{1}{T}) - \frac{\sigma_E^2}{2K^2}(\frac{1}{T})^2]} \quad (I.5)$$

Where E_m and ρ_0 represent the average and standard deviation values of defect level, respectively. Taking advantage of the above three conducting mechanism can well explain the variation rule of FeS_2 resistivity at different temperatures. Besides, researchers also made detailed studies about the Hall test of FeS_2 films. Altermatt et al. [58] applied numerical simulation to investigate the electrical properties of FeS_2 films, such as Hall coefficient, carrier mobility, and a lifetime of majority carriers. They also summarized the parameters of FeS_2 films prepared by different methods. Oertel et al. [59] found the carrier concentration of n-type FeS_2 varied from (10^{18}-10^{21}) cm^{-3}, while the concentration for p-type FeS_2 was lower

than 10^{18} cm^{-3}. When the FeS_2 was alloyed with Ni by ion injection, the carrier type changed from holes to electrons once the Ni concentration exceeded 20% [60]. Ferrer et al. [61] discovered that FeS_2 films obtained by sulfidation of iron films usually exhibited n-type conducting and Hall coefficient was only - 0.57 cm^{-3}. Although the conduction mechanism of FeS2 films is expressing by the above theories, the specific electrical parameters tested in the experiments are closely related to the preparation techniques. Table I.3 summarizes the reported electrical properties of FeS_2 materials prepared by different methods and with different structures. Due to the high conductivity and suitable energy level for the hole extraction, FeS_2 is considered as a promising candidate for the hole transport materials in perovskite solar cells [62].

Table I.3. Reported electrical properties of FeS_2, materials prepared by different technologies.

Preparation method	Shape	Conductivity $(\Omega cm)^{-1}$	Hall mobility(cm^2/V)	Carriers concentration	Conducting type	reference
CVD	Nanoparticles	0.1	20	6.5×10^{18}	P	[63]
Spray pyrolysis	Nanoparticles	0.3	1.5	23×10^{17}	P	[64]
CVD	Nanoparticles	0.97	2.80	5.5×10^{17}	P	[59]
MOCVD	Nanoparticles	0.1	2.4	$\geq10^{20}$	P	[38]
Megnetron sputtering	Nanoparticles	1.3-3.3	2	$10^{20}\times10^{21}$	P	[40, 65]
Electro-deposition	Nanoparticles	_	213	2.9×10^{14}	P	[65]
Sol-gel	Nanoparticles	0.01	32.9-429	1.5×10^{19}	P	[46]
Direct sulfidation	Nanowires	3.7-11.1	0.03	4×10^{21}	P	[20]
Sulfidation of Fe film	Film	_	7.1	2.9×10^{18}	P	[66]

I.3.4. Elastic properties

The elastic properties of iron pyrites have long presented difficulties [67] gave values showing that, in magnitude, the highest elastic constant C_{11} than for any other known substance. Since tungsten [68], diamond [69], and corundum [70] have been shown to have higher values of C_{11}, but remain that FeS_2 should have the large elastic constant. A second notable feature was the negative value of C_{12} and the corresponding positive value of S_{12}. If in the direction of one side of the unit cell, a stretching force is applying, then it produces expansion in a direction perpendicular to that unit cell if S_{12} is positive. Naturally, this is the opposite of what usually happens, as attested by Voigt [67] in the $NaClO_3$ [71]. Also, Doraiswami [72], by using the supersonic waves method, obtained positive values substantially in agreement with Voigt. Because of the high numerical value of the elastic constants C_{11} and C_{44}, iron pyrite scatters relatively little diffuse X-rays. Therefore, more care should be taken than usual to obtain adequate measurements. Besides, the fluorescent K radiation from the iron atoms is the principal difficulty. However, these difficulties were overcoming. A thorough study of iron pyrites would include an investigation of crystals of composition varying over the known range ($FeS_{1.944}$-$FeS_{2.01}$) [73]. The structure may be defective in sulfur atoms or iron atoms relative to the stoichiometric composition. The present crystal was founding to be thermoelectrically negative over to of the copper and to have low specific resistance and a positive temperature gradient of resistance, as reported by Smith [73].

I.4. Iron disulfide applications

Iron disulfide finds applications in the following areas [3, 20, 53, 54, 74, and 75]:

- Solar cells
- Photo electrochemical cells
- Lithium metal sulfide batteries
- Molding compounds
- Production of sulfuric acid
- Photo assisted hydrogen generation
- Photo catalyst

I.5. Thin film

I.5.1. Definition

A thin film has been defined as a low-dimensional material created by condensing, one-by-one, atomic/molecular/ionic species of matter on a substrate, where the thickness of the film is typically less than several microns. Thin films exhibit unique properties that cannot be observed in bulk materials. To this end, many industrial productions in photovoltaic solar cells and electronic components adopt thin-film technology because of its great properties. The basic properties of thin films, such as film composition, crystal phase, and orientation, film thickness, and microstructure, are controlled by the deposition conditions.

I.5.2. Thin film formation mechanism

The formation of a thin film takes place via nucleation and growth processes. The general picture of the step-by-step growth process emerging from the various experimental and theoretical studies can be presented as follows:

1- The unit species, on impacting the substrate, lose their velocity component normal to the substrate and are physically adsorbed on the substrate surface.
2- The adsorbed species are not in thermal equilibrium with the substrate initially and move over the substrate surface. In this process, they interact among themselves, forming bigger clusters.
3- The clusters or the nucleus are thermodynamically unstable and may tend to desorb in time, depending on the deposition parameters. If the deposition parameters are such that a cluster collides with other adsorbed species before getting desorbed, it starts growing in size. After reaching a certain critical size, the cluster becomes thermodynamically stable.
4- The critical nuclei grow in number as well as in size until a saturation nucleation density is reached.
5- The next stage in the process of film formation is the coalescence stage, in which the small islands start coalescing with each other in an attempt to reduce the substrate surface area.
6- Larger islands grow together, leaving channels and holes of uncovered substrate. The structure of the films at this stage changes from discontinuous island type to porous network type. Filling of the channels and holes forms a completely continuous film.

Depending on the thermodynamic parameters of the deposit and the substrate surface, the initial nucleation and growth stages may be described as (a) island type, called Volmer-Weber type, (b) layer type, called Frank-van der Merwe type, and (c) mixed type, called Stranski-Krastanov type. This is illustrated in Fig I.5 [76].

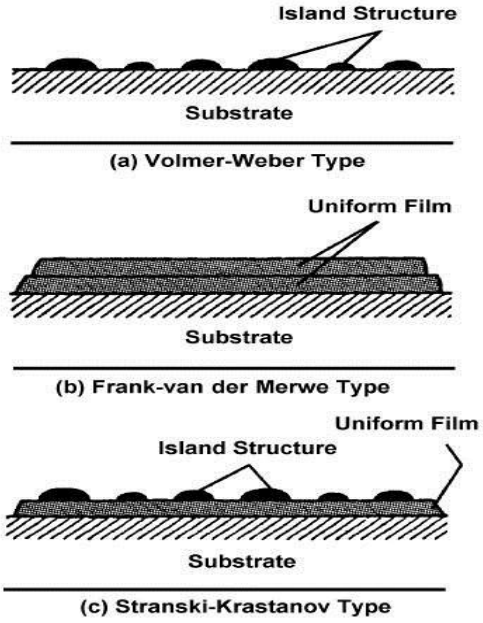

Figure I.5: *Three modes of thin film growth processes* [76].

I.5.3. Deposition of iron disulfide thin film mechanism

☑ As for the synthesis methods of pyrite thin films, up to now, a variety of works have been reported. As by sulfurization of iron films [77-81], the pyrite is prepared in a two-step process; first, the thin iron films evaporate on a substrate, and then exposed to sulfurization. The Spray pyrolysis [82, 83] is also suitable for the deposition of iron pyrite films, by using aqueous solutions of ($FeSO_4$ and $(NH_4)_2S_x$) as precursors for Fe and S, respectively. The aqueous solutions of these precursors are sprayed alternately onto a heated substrate and thus the pyrite is formed on the substrate. Fig I.6 shows the schematic illustration of the spray device.

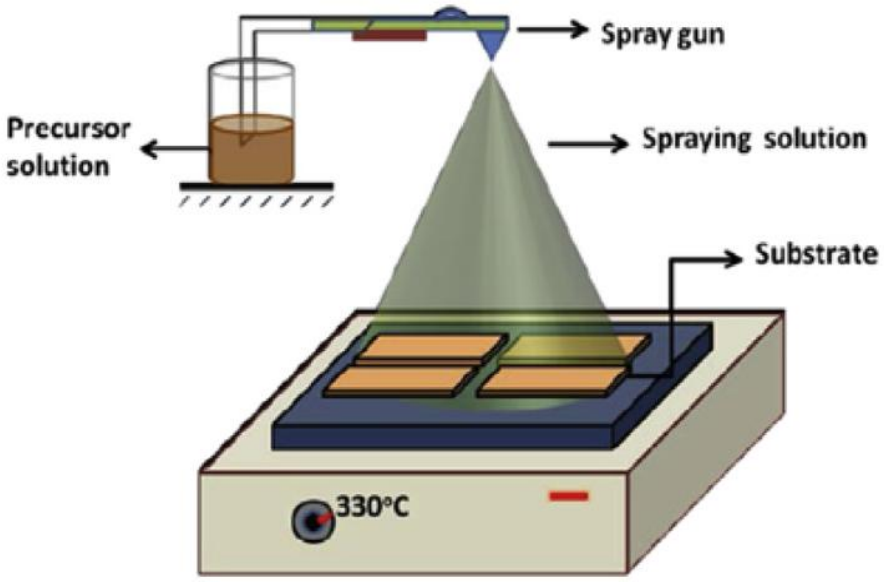

Figure I.6: *Schematic illustration of the spray device* [4].

☑ Thermal evaporation [84– 86] is another technique to prepare pyrite thin films by different procedures such as flash evaporating natural FeS_2 powder or by sulfidation thermally evaporated iron films. The chemical vapor deposition (CVD) method [4] is a direct synthesis, in which FeS_2 can be formed by one step without subsequent sulfidation. It mainly takes advantage of the vapor chemical reactions between selected iron and sulfur sources on various substrates, such as glass, silicon, and molybdenum. Fig I.7 shows the schematic diagram of a chemical vapor deposition (CVD) system.

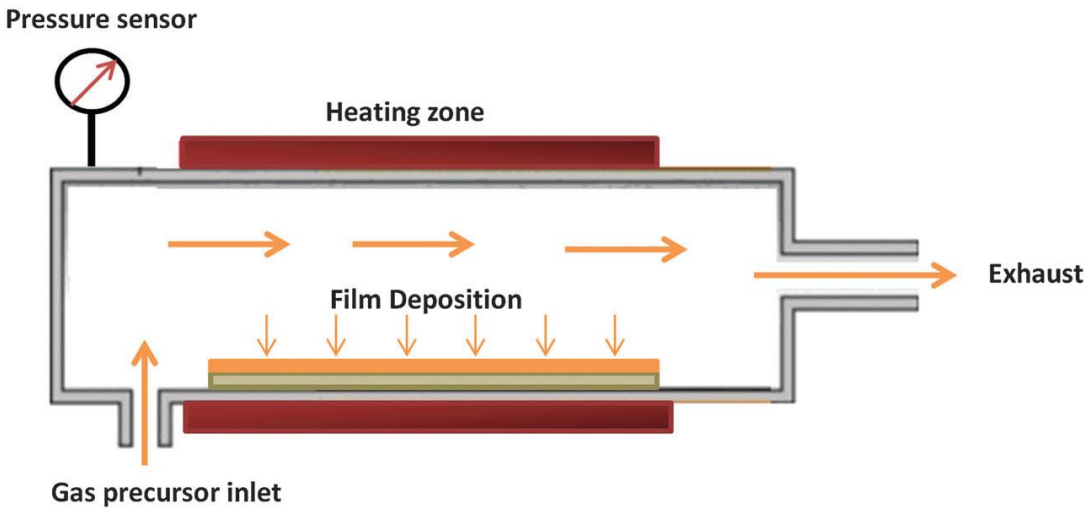

Figure I.7: *Schematic diagram of a chemical vapor deposition (CVD) system* [87].

☑ In 2010, Anuar et al. [88] have deposited FeS_2 thin films using chemical bath deposition (CBD), which is a demanding approach concerning economic considerations. An advantage of this method is that thin films with a large area can be prepared without vacuum, using simple and low-cost equipment (Fig I.8).

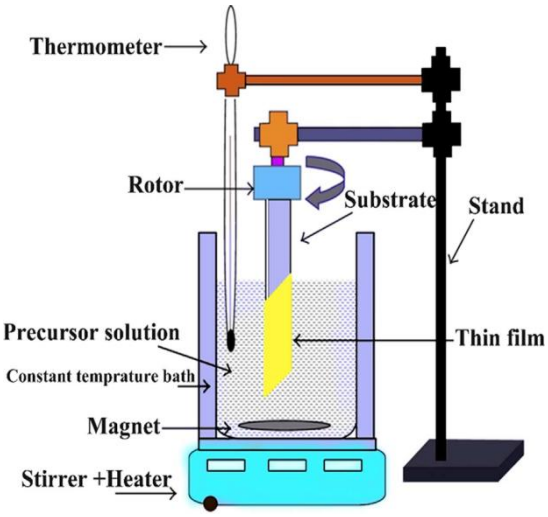

Figure I.8: *Schematic illustration of the chemical bath device* [89].

☑ In 2012, Kaiwen Sun et al. [90] have used a simple and low-cost way to prepare a single-phase and appropriate composition pyrite (FeS_2) thin films via sulfurizing oxide precursor thin films. The oxide precursor (Fe_2O_3) thin films were fabricated by successive ionic layer adsorption and reaction (SILAR) method. The schematic illustration of the experimental process is exposing in Fig I.9.

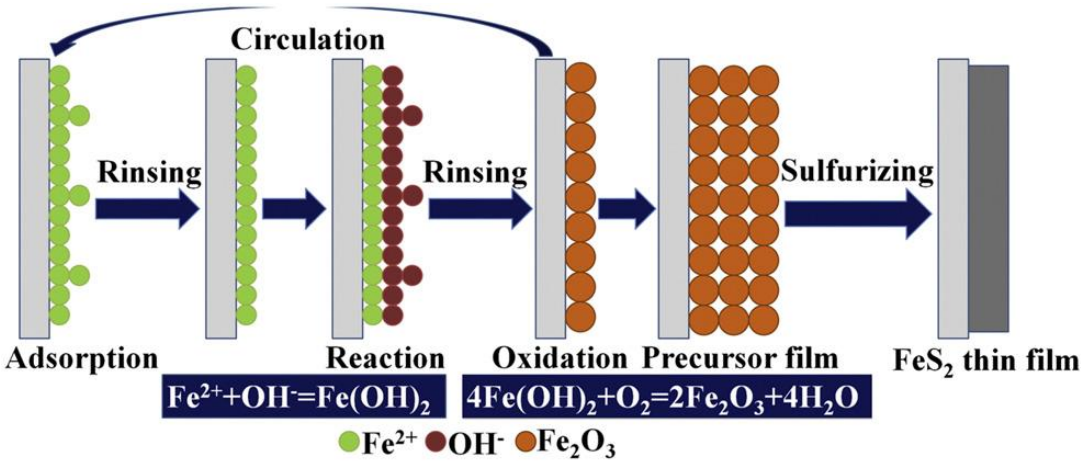

Figure I.9: *Schematic illustration of the formation of FeS_2 thin films* [90].

The possible reactions during the whole procedure are as follows:

$$Fe^{2+} + OH^- = Fe(OH)_2 \quad (1)$$

$$4Fe(OH)_2 + O_2 = 2Fe_2O_3 + 4H_2O \quad (2)$$

$$2Fe_2O_3(s) + 11S = 4FeS_2(s) + 3SO_2(g) \quad (3)$$

I.5.4. Nanostructuration of iron disulfide thin layers

Crystalline structures and their nano-structuration is an emerging research topic in the photovoltaic and electronic component industries, requiring the development of a wide variety of techniques to produce FeS_2-based nanostructures. These techniques can be divided into two categories; physical and chemical processes. These techniques lead to the synthesis of a variety of FeS_2 nanostructures such as nanoparticles, nanowires, nanotubes, and microspheres. According to the difference in their shapes, FeS_2 nanostructures are dividing into 0D, 1D, 2D, and 3D [4]. Fig I.10 (a) shows FeS_2 nanoparticles obtained by Meng et al. [74] using the sol-gel method. Seefeld et al. [91] used a method similar to sol–gel to produce pyrite FeS_2 nanoparticles (Fig I.10 (b)).

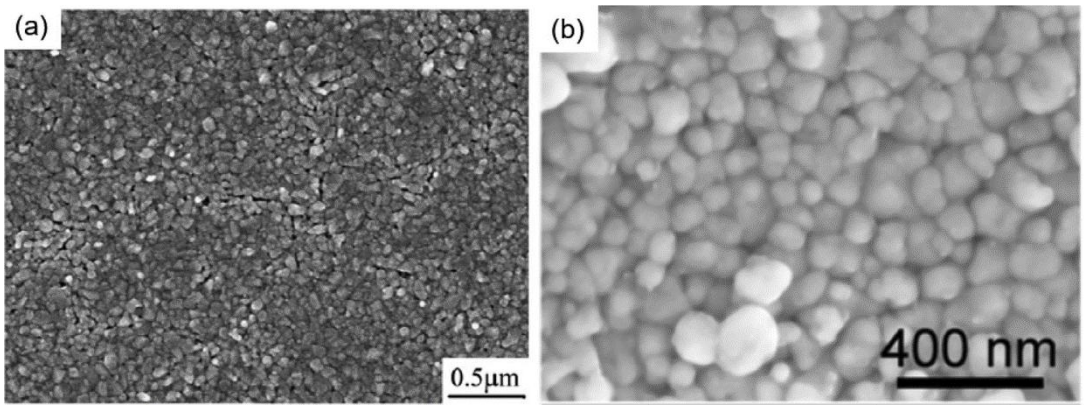

Figure I.10: *SEM images of the FeS_2 nanoparticles by sol–gel method (a) in ref.* [74] *and (b) in ref.* [91].

Kar and Chaudhuri [92] synthesized 1D FeS_2 nanostructures using a solvothermal process. They have controlled the morphologies of FeS_2 nanostructures by changing molar concentrations of precursors, the iron source, and reaction temperatures. Fig I.11 displays various 1D-FeS_2 nanostructures obtained by controlling these experimental parameters.

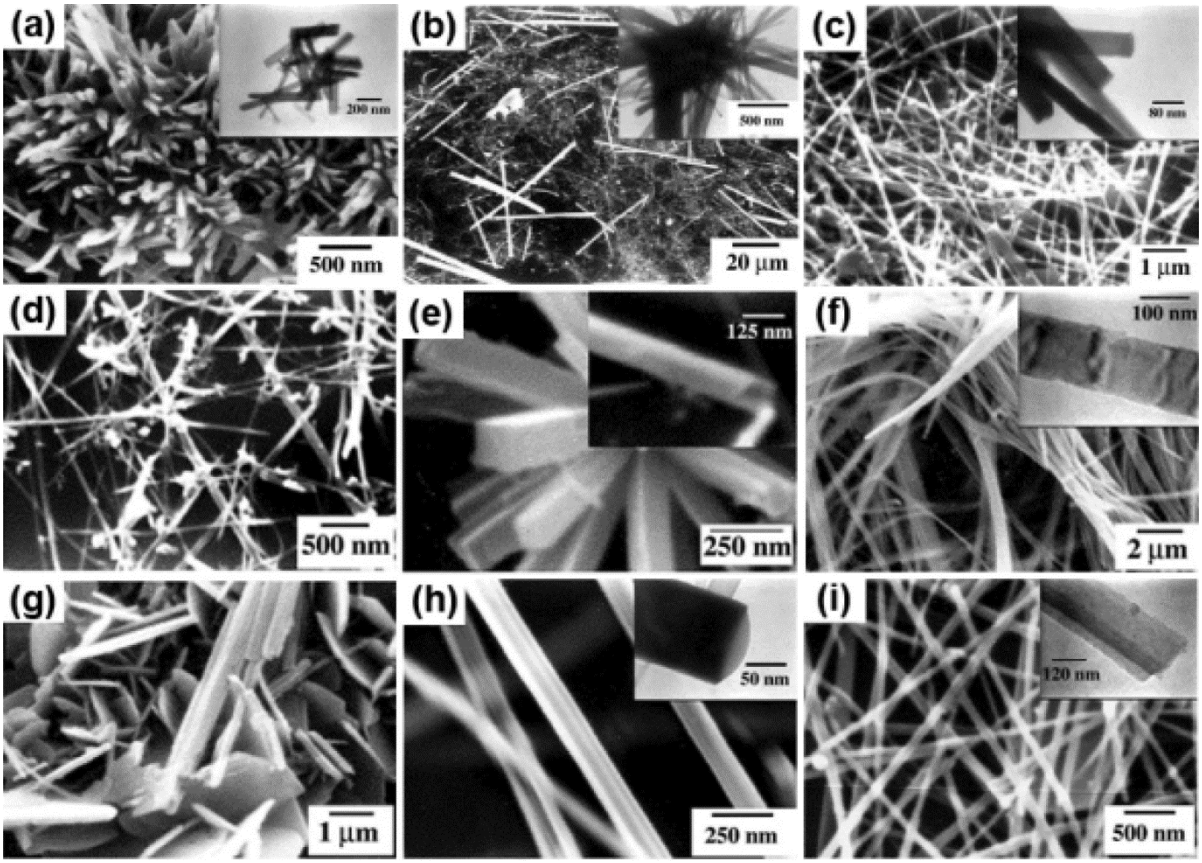

Figure I.11: *SEM images of various 1D FeS_2 nanostructures by controlling iron sources, the molar concentration of precursors and reaction temperature* [92].

Fig I.11 (a-c) synthesized at 180 °C with different iron sources (a) $FeSO_4 \cdot 7H_2O$; (b) $FeCl_3$; (c) $Fe(NO_3)_3 \cdot 9H_2O$; Fig I.8 (d-g) synthesized by using $Fe(NO_3)_3 \cdot 9H_2O$ at different temperature: (d) 150; (e) 180; (f) 210; (g) 230 °C; Fig I.8 (h, i) synthesized by using $Fe(NO_3)_3 \cdot 9H_2O$ at 180 °C with different molar concentration of the precursors: (h) less amount (half) of the precursor; (i) higher molar concentration (double) of the precursors.

Fig I.12 shows the morphologies of developed 2D FeS_2 nanostructures, such as nanoplates and nanosheet. Kirkeminde et al. [93] synthesized FeS_2 nanoplates via the reaction between $Fe(CO)_5$ precursor and polyamine coordinated elemental sulfur solution at 180 °C or higher temperature and aging more than 180 min (Fig I.9 (a)). Hu et al. [94] selectively obtained FeS_2 nanosheets via a one-step hydrothermal method. FeS_2 nanosheets with diameters of ~2μm and thickness of 30 nm were obtained after Fe foil with a purity of 99.99%, and sulfur powder dissolved in deionized water reacted at 160 °C for 12 h (Fig I.9 (b)).

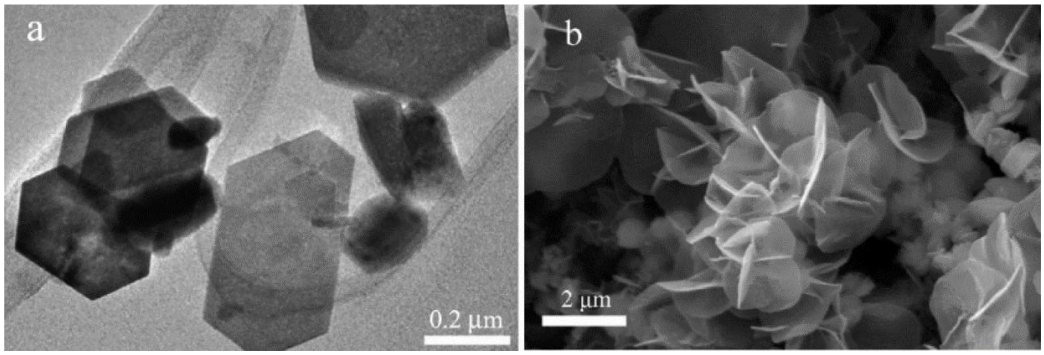

Figure I.12: *SEM images for (a) FeS_2 nanoplates* [93] *and (b) FeS_2 nanosheets* [94].

Li et al. [95] applied a microwave-assisted polyol reduction method to prepare FeS_2 microspherolites with 3-dimensional sizes in the micron scale (Fig I.13). They performed reaction-time dependence experiments to confirm their aggregation-based mechanism. The formation process involved nucleation, growth, and aggregation of the particles.

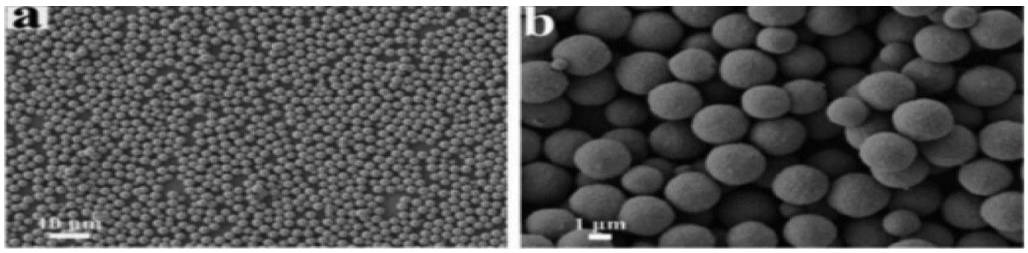

Figure I.13: *SEM images of the FeS_2 microspherolites by microwave irradiation (a) low magnification and (b) high magnification* [95].

Chapter II

Synthesis methods of FeS_2 nanostructures

II.1. Introduction

The performance of FeS_2-based devices is highly dependent on the surface state, the interaction between the interacting media or devices that usually result at the surface or interface. In recent decades, efforts have focused on the preparation, functionalization, and study of FeS_2 nanomaterial applications. Despite this great interest, a comprehensive review of the FeS_2 nanomaterial is insufficient from this perspective. Such a thorough examination, of FeS_2 nanomaterials, would promote the development of this material for the energy research field. The work focuses on the synthesis, properties, modifications, and applications of the FeS_2 nanomaterial, taking into account recent literature [4, 21, 29]. So, the primary objective of this chapter is to explore an updated and encyclopedic overview of FeS_2 nanostructures, which can serve as a source of introduction to this field, with emphasis on this scope of research. It seems reasonable to expect that it will revitalize new ideas and improvements in this and related areas of research. FeS_2 nanostructures have been synthesized, with some different compositions and phases. Most research has focused on the synthesis of these nanomaterials. Several publications [41–52] have described effective synthesis routes to control the shape morphology, stability as well as the dispersity. Many methods knowing: hydrothermal, hot injection, solvothermal, and sulfidation, have been used to prepare high-quality FeS_2 nanomaterials. The distinctive and representative examples for the discussion of each synthesis routes are presented. However, there barely are low cost and simple methods with good stoichiometric controllability reported. Consequently, there is a significant research interest in developing simple and inexpensive techniques for preparing thin layers of pyrite of appropriate composition (FeS_2). The objective of this work is to focus on one of the simplest methods to fabricate nanostructured FeS_2 thin films. Thus, the discussion below will focus on the deposition methods that will be used in this study to synthesize pyrite thin films.

II.2. Deposition techniques

The chemical vapor deposition method offers many advantages, the most important of which are low cost, excellent step coverage, and uniformity. Also, the chemical bath deposition as a method for thin-films and nanostructures preparation is the best approach for economic considerations. The advantage of this method is that using simple and low-cost equipment giving high-quality nanostructures. However and due to these advantages, the focus will be placed on these two methods.

II.2.1. Chemical Vapor Deposition (CVD)

Chemical vapor deposition is an axis of processes whereby a solid material is deposited from vapor by a chemical reaction occurring on or in the vicinity of a normally heated substrate surface. The resulting solid material is in the form of a thin film, powder, or single crystal. By varying experimental conditions, including substrate material, substrate temperature, and composition of the reaction gas mixture, total pressure gas flows, etc., materials with a wide range of physical, tribological, and chemical properties can be grown. A characteristic feature of the CVD technique is its excellent throwing power, enabling the production of coatings of uniform thickness and properties with a low porosity even on substrates of complicated shape. Another important feature is the capability of localized or selective deposition, on patterned substrates [96].

There exists a multitude of CVD processes, such as atmospheric pressure CVD (AP-CVD), low-pressure CVD (LP-CVD), metal-organic chemical vapor deposition (MO-CVD), ultrahigh vacuum CVD (UHV-CVD), hybrid physical-chemical vapor deposition (HP-CVD), etc. The choice between these different methods is making by considering several parameters such as the deposition rate, film uniformity, electrical and mechanical properties, the substrate temperature, and the chemical composition of the films. CVD and related processes are employed in many thin-film applications, including dielectrics, conductors, oxidation barriers, conductive oxides, epitaxial layers for microelectronics, production of solar cells, high-temperature fiber composites, particles of well-defined sizes, etc [96]. As for the synthesis of pyrite thin films with the CVD Technique, a variety of works have been reported. Leith Samad et al. [31] synthesized phase-pure iron pyrite thin films via chemical vapor deposition. Ben Meester et al. [54], D. M. Schleich, and H.S.W. Chang [97] have prepared iron disulfide thin films by low-pressure CVD (LP-CVD). B. Thomas et al. [98] prepared thin films of pyrite by low-pressure metal-organic chemical vapor deposition (LP-MOCVD). Naoyuki Takahashi et al. [99] prepared single crystal pyrite thin films by chemical vapor deposition under atmospheric pressure (AP-CVD).

In every CVD process, gaseous reactants are admitted into a reactor (Fig II.1). Near or on a heated substrate surface the following chemical reaction occurs:

Gaseous reactants (g) → Material particles (s) + Gaseous products (g)

Five important reaction zones related to gas flows and temperature are developed during the CVD process, as shown in Figure II.2. The properties of CVD materials are affected by the

interacting processes occurring in these reaction zones, in which the main gas flow (the reaction gas mixture) passes over the substrate/coating surface. Fluid dynamics of the process results in a more or less stagnant boundary layer occurring in the vapor adjacent to the substrate/coating. During the deposition process, the gaseous reactants and products are transported across this boundary layer. In reaction zone 1 (Fig II.2), as well as in the main gas stream, homogeneous reactions may occur in the vapor, which may lead to undesirable homogeneous nucleation characterized by a flaky and non-adherent coating. Heterogeneous reactions occur in the phase boundary vapor/coating (zone 2). These reactions typically determine the deposition rate and properties of the coating. Relatively high temperatures can be used during CVD, leading to various solid-state reactions (e.g. phase transformations, recrystallization, and grain growth) that can occur in zones 3–5. In zone 4, which is a diffusion zone, it is possible to form various intermediate phases. The reactions in this zone are important for the adhesion of the coating to the substrate [96].

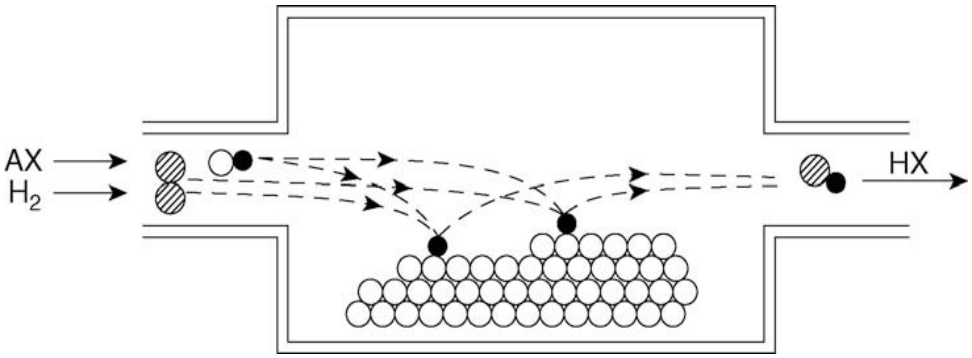

Figure II.1: *The principle of CVD* [96].

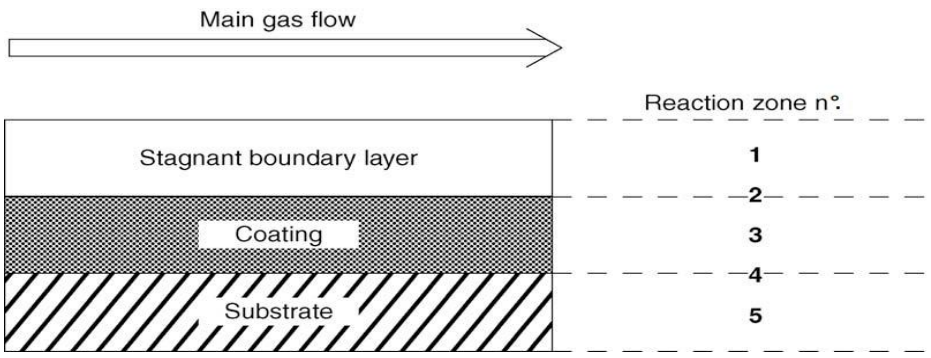

Figure II.2: *Important reaction zones in CVD* [96].

As an application, FeS_2 thin-films or nanostructures were fabricated using CVD techniques. $FeCl_3$ and Di-tert-butyl disulfide used as iron and sulfur precursors [31]. In other

side, FeS_2 thin films were deposited by using single precursor in which iron nitroprusside $Fe[Fe(CN)_5(NO)]_{1.5}H_2O$ was treated with sodium sulfide due to the high sensitivity of nitroprusside towards the sulfide group [100]. The phase and morphology of FeS_2 material can be tuned with varying reaction conditions producing a shape variety of FeS_2 nanomaterial [101].

A more detailed picture of the basic physicochemical steps in an overall CVD reaction is illustrated in Figure II.3, which indicates several key steps [102]:

1. Evaporation and transport of reagents (i.e. precursors) in the bulk gas flow region into the reactor;
2. Gas-phase reactions of precursors in the reaction zone to produce reactive intermediates and gaseous by-products;
3. Mass transport of reactants to the substrate surface;
4. Adsorption of the reactants on the substrate surface;
5. Surface diffusion to growth sites, nucleation, and surface chemical reactions leading to film formation;
6. Desorption and mass transport of remaining fragments of the decomposition away from the reaction zone.

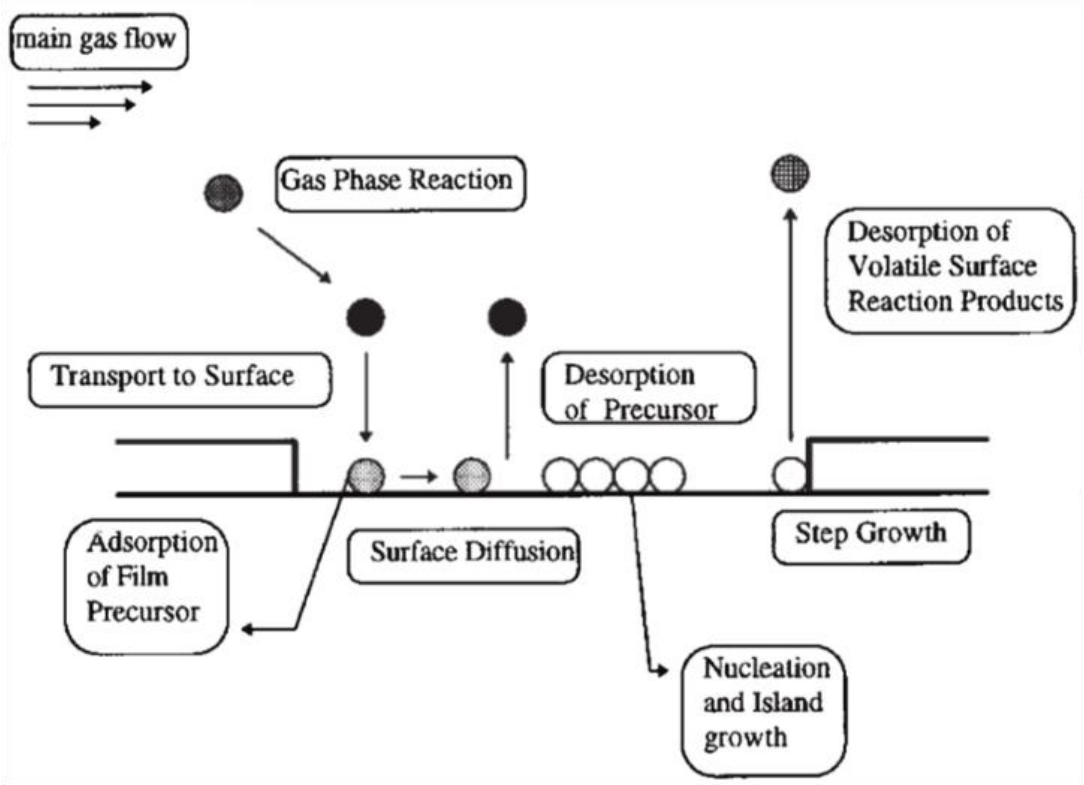

Figure II.3: *Precursor transport and reaction processes in CVD* [102].

II.2.2. Chemical Bath Deposition (CBD)

Chemical bath deposition (CBD) is an old technique, also called a solution growth technique. In 1835, Liebig presented the first report of the deposition of silver using this method. Earlier, CBD has been limited to the deposition of lead compounds PbS and PbSe. The range of metal chalcogenide films deposited by CBD has been gradually developed, particularly in the 1980s. In 1982, about twenty metal chalcogenides were synthesized by this technique. Nowadays, the number exceeds 50, most of which are semiconductors. The reason for this growing interest is due to the advantages of the attractive technology of the CBD [103].

Among the many different methods available to deposit films of semiconductors, chemical bath deposition must rank as conceptually the simplest. CBD is a technique in which thin semiconductor films are deposited on substrates immersed in dilute solutions containing metal ions and a source of hydroxide, sulfide, or selenide ions. Control of the temperature (usually below 100 °C), pH, and concentration of the solution induces a solid phase to exsolve and form a film on the substrate (of any shape and size), often without any subsequent heat treatment [104–106]. The chemical bath deposition technique is well suited for producing large-area thin films for solar energy-related applications. As attested by the literature, a variety of works have been reported on the deposition of pyrite thin films [88, 107–109].

To understand chemical bath deposition processes, and thereby to be able to exert control over aspects such as the growth rates, structures, and properties of the deposited films, it is helpful to divide the topic into three general areas [104]:

1. Solution chemistry
2. Substrate effects
3. Process control

II.2.2.1. Solution chemistry

To deposit a $MX_{n/2}$ compound via CBD, the deposition medium will consist of one or more salts of metal M^{n+} and a source for the chalcogenide X (X = O, S, Se) in aqueous solution. Products containing multiple metals are relatively easily obtained when a specific cation stoichiometry is not required (doped materials or solid solutions) and the metals have similar precipitation behavior at a given temperature and pH. A complexing agent (also called the complexing agent) can be added as a means (in addition to adjusting concentration, temperature, and pH) to control the rate of the solid formation. Typically, complexants supply

ligands for the metal, and the greater their affinity for the metal relative to that of the chalcogenide, the more the complexant helps slow down the hydrolysis reactions that lead to the formation of the solid phase. When the desired compound contains multiple metals whose hydrolysis rates differ widely under a chosen set of deposition conditions, a complexant can be particularly useful for slowing the deposition kinetics of the more readily hydrolyzed species. The concentration of the complexant is usually chosen to be a predetermined ratio of the concentration of the metal precursor [104].

For non-oxidized films, the chalcogenide source is present at a diluted concentration (typically 0.01-0.1 M). This concentration is an additional parameter to control the deposition rate of the film. Therefore, the sulfide, thiourea ($(NH_2)_2CS$), thioacetamide (CH_3CSNH_2), or soluble salts of thiosulfate ($S_2O_3^{2-}$) are desired precursors S^{2-} ions source. The addition of chalcogenide precursor to the solution will primarily determine the concentration [X^{2-} (aq)] of the free chalcogenide ion. One of the parameters, which determine the degree of supersaturation of the solution, tends to produce the desired solid. Although pH and temperature allow some modulation of the free chalcogenide concentration, one of the easiest ways to slow down the rate of solid production is simply to reduce the starting concentration of the chalcogenide source. The increase of the temperature motivates the chalcogenide source decomposition, thus accelerate the formation of the solid. Besides, increasing the concentration of metal salt increases the rate of reaction and increases the amount of material able to be deposited from the solution [104]. K. Anuar et al. [108] got to the conclusion that the grain sizes of FeS_2 films prepared at higher pH values are large than those deposited at lower pH values. Fig. II.4 illustrates the effect of solution pH and metal concentration [M] on the tendency of a solution to resolve a solid phase.

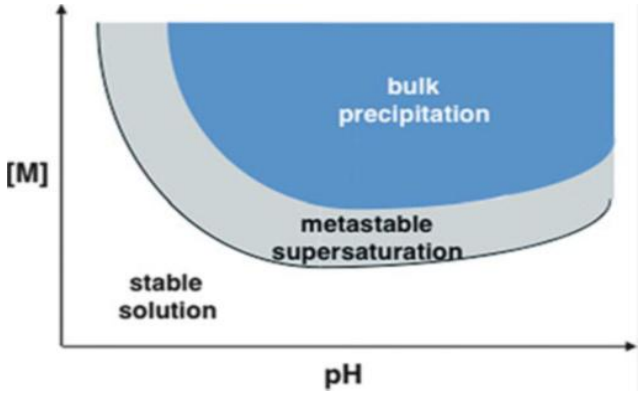

Figure II.4: *Schematic illustration of the effect of solution pH and metal concentration [M] on the tendency of a solution to resolve a solid phase* [104].

The degree of supersaturation, which is a measure of the degree to which the concentrations of the free ions in solution exceed their solubility limits, it plays a central role in film formation. Supersaturation is most often controlled by the concentration, pH, and temperature of the solution. When film growth occurs by particle attachment, the degree of supersaturation dictates the size, population, and rate of formation of the particles making up the film. When the pH and concentration place the solution deep in the field labeled "bulk precipitation" in Fig II.4, film forms rapidly in the solution. In the field labeled "metastable supersaturation," solid may form on any solid surface that lowers the thermodynamic barrier to nucleation. Ideally, the only such surface would be the substrate, but in practice, it can be hard to avoid nucleation on other surfaces (including container walls and adventitious particles in the solution) and to maintain the solution conditions continuously (and with spatial uniformity) in the metastable condition. Films from less heavily supersaturated solutions typically grow more slowly but may ultimately reach higher thickness. Overall, the growth rate is determined by supersaturation (temperature, concentration, and pH), while thickness is limited by the supply of reactants (starting concentrations and avoidance of bulk precipitation) [104].

The presence of organic additives in the deposition liquid plays a significant role in the control of the morphology of the formed particle, and consequently, the film. The additives can be adsorbed preferentially on specific faces of the inorganic crystal, inhibiting the growth of those faces. The uncoated faces then grow further, conferring unusual morphologies [110, 111]. Also, crystallographically non-selective adsorption of the additives leads to "miniaturization" of the formed crystallite by slowing the growth rate in all directions. Many of the additives that adsorb onto crystal surfaces have functional groups similar to those found on effective complexing agents, especially carboxylic acid, alcohol, amide, and ether groups. In some cases, the role of the organic additive is not exclusively to control the growth rate of certain crystal faces, but also to promote the formation of an intermediate amorphous phase during the crystal growth. The presence of these amorphous particles can reduce the degree of supersaturation of the solution, suppressing the rapid formation of the initial crystals. The amorphous phase then dissolves, and nanocrystals are forming. The amorphous particles contain metal ions that are gradually released, promoting a more controlled crystallization process [104].

II.2.2.2. Substrate effects

The chemical nature of the substrate surface and its interactions with the depositing solid and the liquid deposition medium together influence the film's growth rate and morphology. The CBD mechanisms, as shown in (Fig II.5), can be achieved through two different processes:

- Dissolved ionic species may attach to the substrate according to an ion by ion growth mechanism. In this case, heterogeneous nucleation leads to the directed growth of nuclei of the inorganic phase on the substrate.
- Colloidal particles may form in the solution by hydrolysis and condensation reactions of the dissolved species and subsequently be attracted to the substrate by electrostatic or van der Waals interactions. Here nucleation in solution is involved and usually results in a polycrystalline film with random crystal orientation.

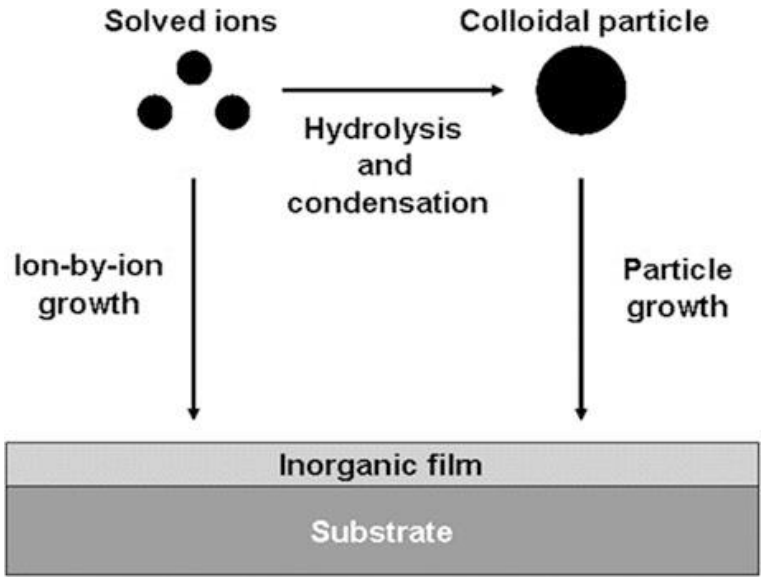

Figure II.5: *Mechanisms for the formation of inorganic films from aqueous inorganic solutions* [104].

Both mechanisms can occur simultaneously, or ion by ion growth can be following by particle attachment. Transparency of the solution does not rule out the possibility of the film growth by particle attachment. The presence of particles in solution also does not exclude the possibility of the film formation by nucleations and heterogeneous growths on the substrate. In practice, it is usually not possible to determine which process dominated the formation of a

specific film from the nature of the deposition medium alone, or by examining the film's microstructure ex situ [104].

When a supersaturated solution remains stable against precipitation for a very long time unless, specifically, a prepared substrate is present to promote the film formation, nucleation and growth is probably the dominant mechanism of deposition. In contrast, when particles are known to be present in the solution, the occurrence or absence of film formation correlates with the nature of the electrostatic interaction between the substrate and the depositing film. The particle attachment is strongly implicating as a primary mechanism of film deposition. These electrostatic interactions are, first, governed by the zeta potentials of the substrate and the solid phase, which in turn depend on the pH of the surrounding liquid phase. When the pH of the solution is such that the zeta potentials of two film surfaces are opposite in sign, an electrostatic attraction is expecting between them, and repulsion when the zeta potentials have the same sign (Fig II.6). The condition for electrostatic attraction is fulfilling when the pH of the solution is between the isoelectric points, IEP_1 and IEP_2, of the two surfaces (Fig II.6) [104].

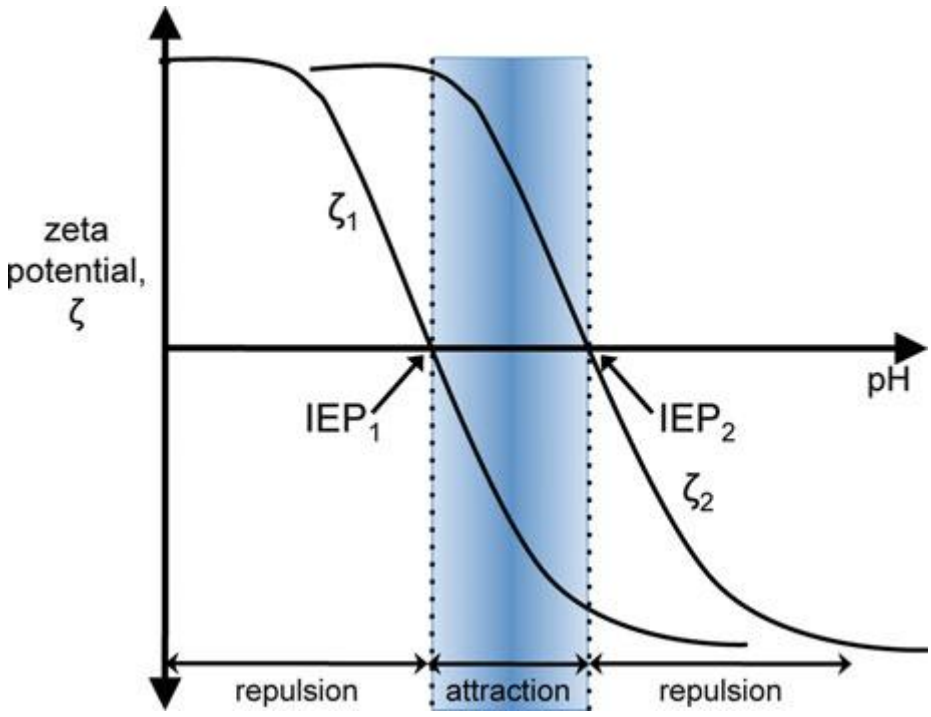

Figure II.6: *Schematic illustration of the effect of the zeta potentials (ζ1 and ζ2) of two adjacent surfaces on the nature of the electrostatic interaction between them* [104].

A significant recent trend in research on the low-temperature deposition of thin films from liquid media has been used for organic eliminations of substrate surfaces to promote the

formation of films. To this end, it can achieve, for example, with surfactants, polyelectrolyte bilayers, and organic self-assembled monolayers (SAMs). SAMs are ultra-thin layers (typically 2.5 nm or less) formed via the spontaneous attachment of hydrocarbon-based surfactant molecules onto a substrate, comprising structurally ordered, two-dimensional arrays [112, 113].

When the surface treatment used to promote film growth is selectively applied to specific regions of the substrate, the subsequent film deposition can be made to conform to that spatially predetermined arrangement, leading to what is called patterned deposition. Patterned functionalization of a substrate can be achieved in the way the functionalization is first applied to the surface, through microcontact printing of a surfactant with what amounts to a "rubber stamp" [114]. Another approach is to shine UV light through a photomask onto a uniformly functionalized surface, either to alter the functional group photochemically or to cleave the adsorbed species from the surface. The resolution that can be achieved in the functionalized pattern can be well into the nanometer scale, depending on the technique used (electron-beam etching, photolithography, etc.). The resolution of the deposited film itself is usually less fine than that of the patterned functional layer. The ability of a liquid to permeate porous structures and to coat fibers, particles, and other shapes with relatively concentrated precursors for solid films is a powerful advantage of CBD approaches [104].

II.2.2.3. Process control

In its simplest form, a CBD process involves a single isothermal immersion of a substrate in a precursor liquid that does not flow the desired film. Even if no external modifications have been imposed on the system (e.g. no reagents are added to the deposition medium), parameters of the solution that affect the deposition process are far from static. In particular, once a film has begun to form, the supersaturation of the solution begins to decrease, and eventually reaches a level at which nucleation of new particles stops (although the growth of existing particles may continue). The pH may significantly change from the initial value, usually in a direction that slows particle nucleation and growth. As solid nucleates and grows (on the substrate, in the solution, or both), solid-solid interactions become more important: e.g. adjacent particles may agglomerate via van der Waals or other interactions, causing continuous changes in the number, size, and spatial distribution of solid particles. Overall, for a single immersion deposition, there is usually an "incubation" period during which there is no film growth. Afterward, this is following by a growth period (which

may have an increasing growth rate followed by a decreasing growth rate). Then, the growth stops once oversaturation has fallen below a critical level. For avoiding the continuous change in solution concentration and pH is to monitor and adjust these parameters periodically or continuously to maintain desired values. Automated electronic systems for maintaining constant pH ("pH-stats") are readily available for small- and large-scale depositions. Sensors are commercially available for continuous measurement of the concentrations of some metal ions in the deposition medium.

When a reactant is added to a solution, spatial gradients in supersaturation will occur. This can lead to inadvertent local precipitation and other inhomogeneities at the site of the addition until the added substance is uniformly mixed into the solution. One way of avoiding this situation, in solutions where a rise in pH can be used to trigger the formation of the solid, is to add urea ($(NH_2)_2CO$) to the solution before heating. In aqueous solutions at temperatures between ~40 and ~80 °C, urea will decompose to form ammonia and carbon dioxide. The net effect is a steady rise in pH, occurring uniformly throughout the solution [104].

II.2.2.4. CBD advantages and limitations

CBD technique enjoys several advantages [103]:

- It is relatively simple and safe due to the application over a wide range of easy chalcogenide compounds preparation.
- The flexibility in the substrate choice.
- It is a useful and excellent technique for nanomaterial preparations.
- It allows the deposition of homogeneous, adherent, and reproducible thin films over a large surface.
- It is carried out at low temperatures as well as relatively high temperatures.
- It is a slow process, in which the reaction time required is sometimes several hours or even tens of hours. This may favor the crystallites size and orientation control.

Despite these advantages, CBD has some limitations. For example, it remains challenging to synthesize multicomponent materials whose individual components precipitate at widely differing pH or temperature, or when the choice of complexants for the metals is limited. In the as-deposited state, the films may contain residual components from the precursor solution. They are often not completely crystallized. As a result, the films often do not exhibit the same physical properties as crystalline sintered materials [104].

Chapter III

FeS_2 Characterization Techniques

III.1. Introduction

Many characterization techniques that can provide information on the studied samples, such as structure, morphology, chemical composition, topography and other various properties are used. In this chapter, we will therefore describe the main techniques used for the characterization of FeS_2 thin films.

So, films crystal structure were inspected using grazing incidence X-ray diffraction (GIXRD) with the glancing angle of 0.8° and a step of 0.05° in 2θ spectra. The measurements are achieved by high-resolution X-ray Bruker D8 Advance diffractometer using Cu-Kα1 monochromatized radiation source with $\lambda_{K\alpha1}$ = 1.54 Å. Raman measurements were performed at room temperature using 325 nm Ar^+ laser wavelength (Horiba Jobin-Yvon Raman). The samples are irradiating in 1800 grooves/mm optical grating during 20 s. The Nicolet FTIR spectroscopy was used within an IR source and KBr beam splitter to give the accurate phase composition of the deposited film.

Films morphology is viewing by JEOL-JSM-7610FPlus Schottky Field Emission Scanning Electron Microscope (SFE-SEM). The equipment can achieve a better resolution using a voltage range from 0.5 kV to 15 kV, a semi-in-lens type objective, and high power optics of irradiation system (HPO). UV–Vis–NIR recording spectrophotometer CARY 500 from 350 to 2100 nm wavelength range is used for the measurements of reflectance diffuse.

III.2. X-ray Diffraction (XRD)

X-Ray diffraction (XRD) is a non-destructive and highly quantitative technique that has been extensively used in the investigation of thin films. The XRD method is used to analyze structure parameters such as microstrain, crystallite size, and dislocation density. XRD analysis is also employed to identify details about phase compositions, crystal preferred orientations, and crystal defect concentrations [115]. The principle of the method is based on the diffraction of X-rays by periodic atomic planes and the angle or energy-resolved detection of the diffracted signal. The geometrical interpretation of the XRD phenomenon (constructive interferences) has been given by W.L. Bragg. Fig III.1 gives the details about the geometrical condition for diffraction and the determination of Bragg's law (Eq III.1).

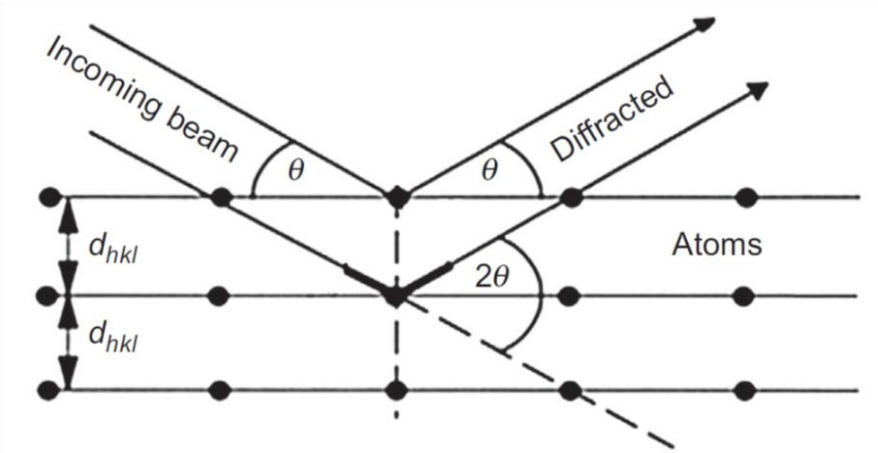

Figure III.1: *Geometrical condition for diffraction from lattice planes* [116].

$$n\lambda = 2d_{hkl}\sin(\theta) \qquad \text{(III. 1)}$$

n is the order of diffraction, λ the wavelength of the incident beam in nm, d_{hkl} the lattice spacing in nm and θ the angle of the diffracted beam in degree.

Recorded diffraction patterns contain additive contributions of several micro- and macrostructural features of a sample. With the peak position, lattice parameters, space group, chemical composition, macrostresses, or qualitative phase analysis can be investigated. Based on the peak intensity, information about crystal structure (atomic positions, temperature factor, or occupancy) as well as texture and quantitative phase analyses can be obtained. Finally, the peak shape gives information about sample broadening contributions (microstrains and crystallite size) [116]. Diffractometer D8 Advance Brucker shown in Fig III.2 will be used for the structural analysis of FeS_2 thin films.

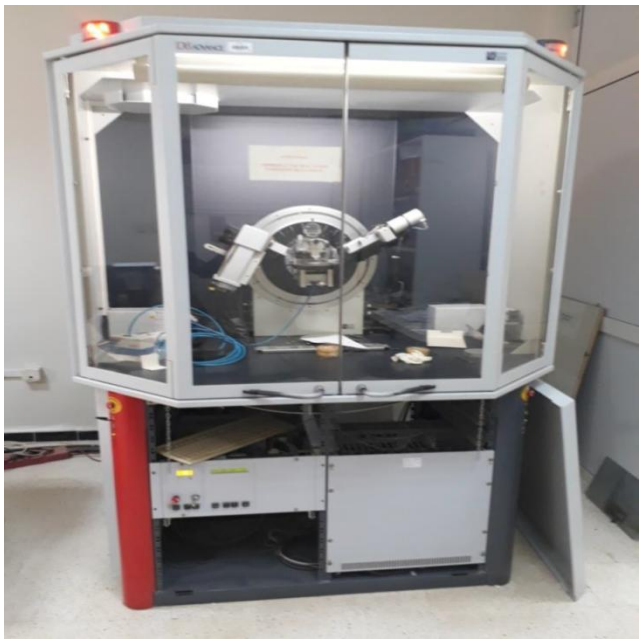

Figure III.2: *Diffractometer D8 Advance Brucker (CDTA).*

III.3. Field Emission Scanning Electron Microscopy (FE-SEM)

Scanning electron microscope (SEM) is a technique used in surface analysis. It analyzes the morphology of the surface and the chemical composition of the solid matter by scanning the surface with a focused beam of electrons. The SEM works by a focused beam of high-energy electrons (primary electrons (PEs)) to generate a variety of signals at the surface of solid specimens (Fig III.3). Among these signals, there are electrons [Auger electrons, secondary electrons (SEs), and backscattered electrons (BSEs)], X-rays (characteristic X-rays and Bremsstrahlung X-ray radiation), light (ultraviolet, visible, and infrared), heat, electrons conducted through the sample, and electrons absorbed by the sample. With some of these signals, it is possible to observe and characterize the sample in terms of its (1) surface morphology, (2) structural organization, and (3) chemical composition [117].

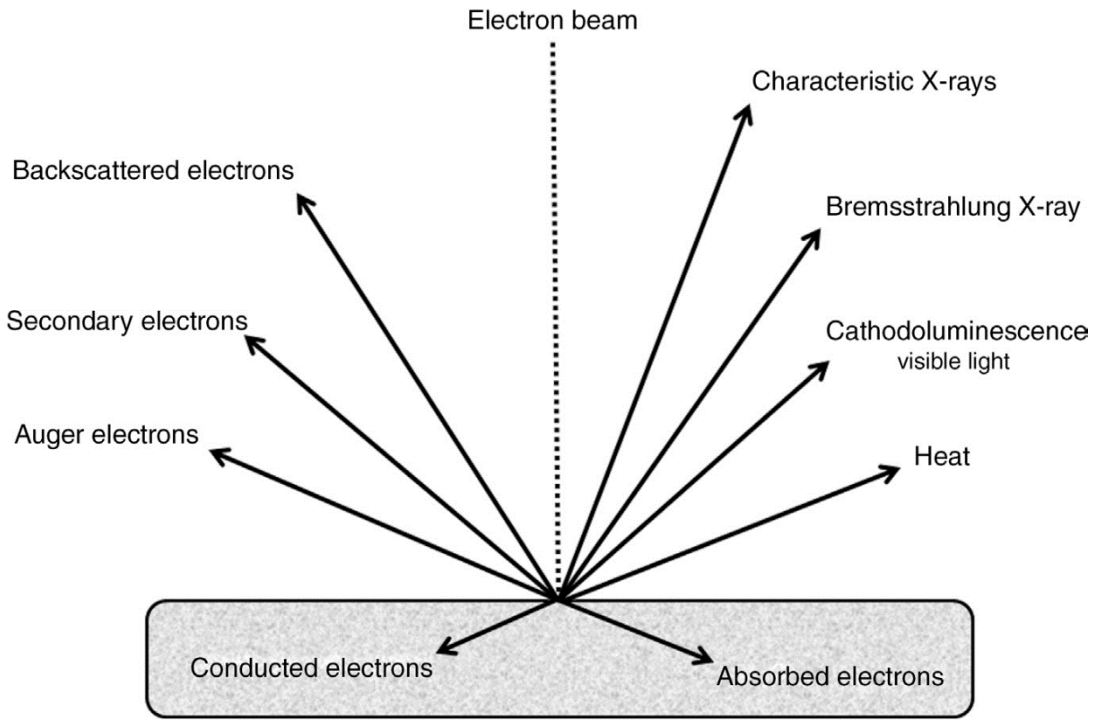

Figure III.3: *Main signals emitted as a result of the interaction between the electron beam and the sample* [117].

Secondary electrons and backscattered electrons are commonly used for imaging samples. The Secondary electrons are a result of inelastic scattering of PEs with weakly bonded electrons of the outer shells of atoms in the whole interaction volume. They possess low energy of 3 – 50 electron volts (eV). Thus, only SEs from a volume close to the surface escape from the material and can be collected and amplified through appropriate detectors.

The secondary electrons are most valuable for showing the morphology and topography of samples. Backscattered electrons are generated by elastic scattering of PEs when they interact with sample atoms. Due to much higher energy than SEs (60% – 80% of the energy of the PEs), they can escape from deeper regions of the interaction volume. The signal that is usually detected by a semiconductor device is strongly dependent on the average atomic number of the interacting atoms. The backscattered electrons are most valuable for illustrating contrasts in composition in multiphase samples [118, 119].

The field emission scanning electron microscope (FE-SEM) is suitable for observing structures as small as 1 nm on the surface of material. The magnification of observation can be adjusted and considered based on the requirements [118]. An ultra-high-resolution Schottky Field Emission Scanning Electron Microscope developed by JEOL, will be employed for the analysis of FeS_2 thin films (Fig III.4).

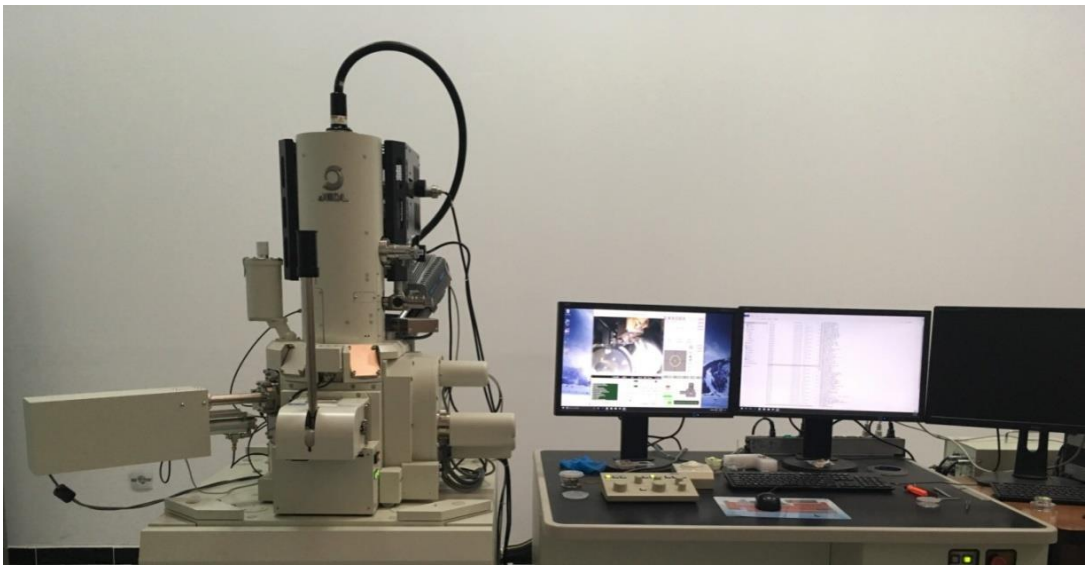

Figure III.4: *Field emission scanning electron microscope (CRTSE).*

III.4. Raman spectroscopy

Raman spectroscopy is a scattering technique. It is based on the Raman Effect, i.e., the frequency of a small fraction of scattered radiation is different from the frequency of the monochromatic incident radiation. It is based on the inelastic scattering of incident radiation through its interaction with vibrating molecules. When monochromatic electromagnetic radiation of energy, $h\nu_0$, is incident upon a sample, it may be reflected, absorbed, or scattered in all directions. Much of this scattered radiation has a frequency that is equal to the frequency

of incident radiation and constitutes Rayleigh scattering. Only a small portion of scattered radiation is inelastic (approximately 1×10^{-7} of the scattered light) and has a frequency ($h\nu_0 + h\nu$ or $h\nu_0 - h\nu$) different from the frequency of the incident radiation ($h\nu$ is the energy difference between vibrational states). The scattered radiation having a lower frequency ($h\nu_0 - h\nu$) is called Stokes lines, and that having a higher frequency ($h\nu_0 + h\nu$) is called anti-Stokes lines, as shown in Fig III.5. This change in wavelength of the scattered photons due to changes in the polarizability of the molecules provides the structural information of the sample. Scattered radiation is usually measured at the right angle to incident radiation. Stokes shifted Raman bands involve the transitions from lower to higher energy vibrational levels and therefore, Stokes bands are more intense than anti-Stokes bands and hence are measured in conventional Raman spectroscopy while anti-Stokes bands are measured with fluorescing samples because fluorescence causes interference with Stokes bands. The magnitude of Raman shifts does not depend on the wavelength of incident radiation, but Raman scattering depends on the wavelength of incident radiation [120,121].

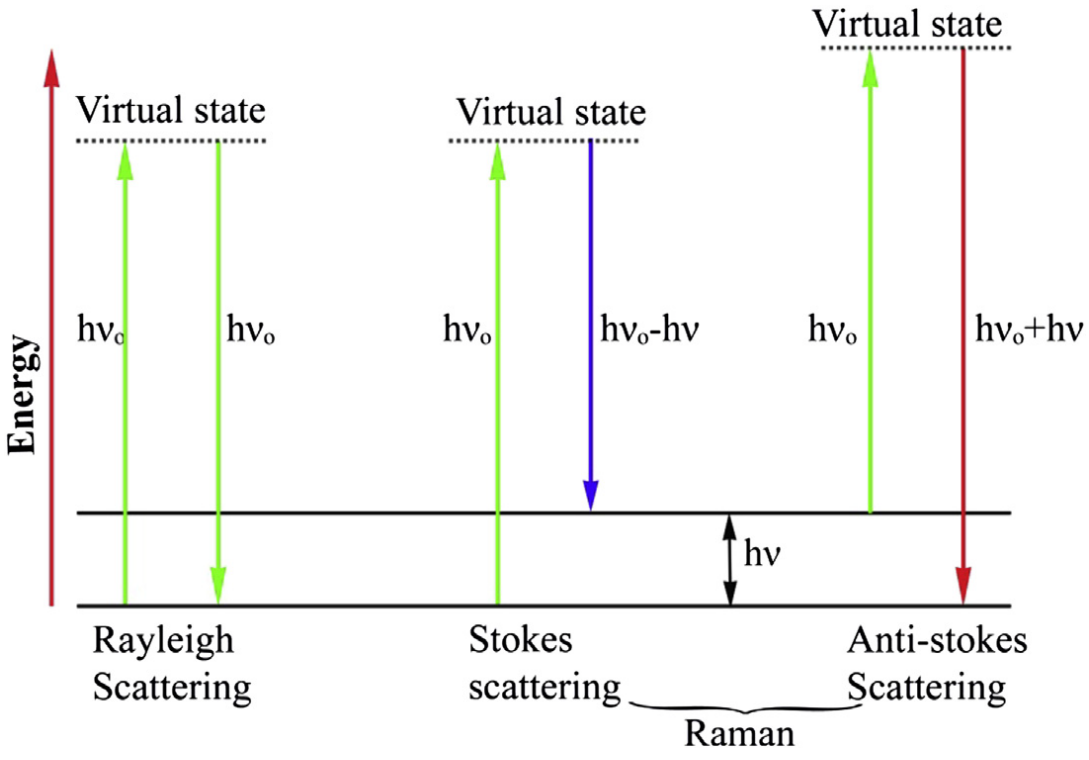

Figure III.5: *Rayleigh and Raman scattering* [121].

The Raman spectroscopy shown in figure III.6 will be used in this study.

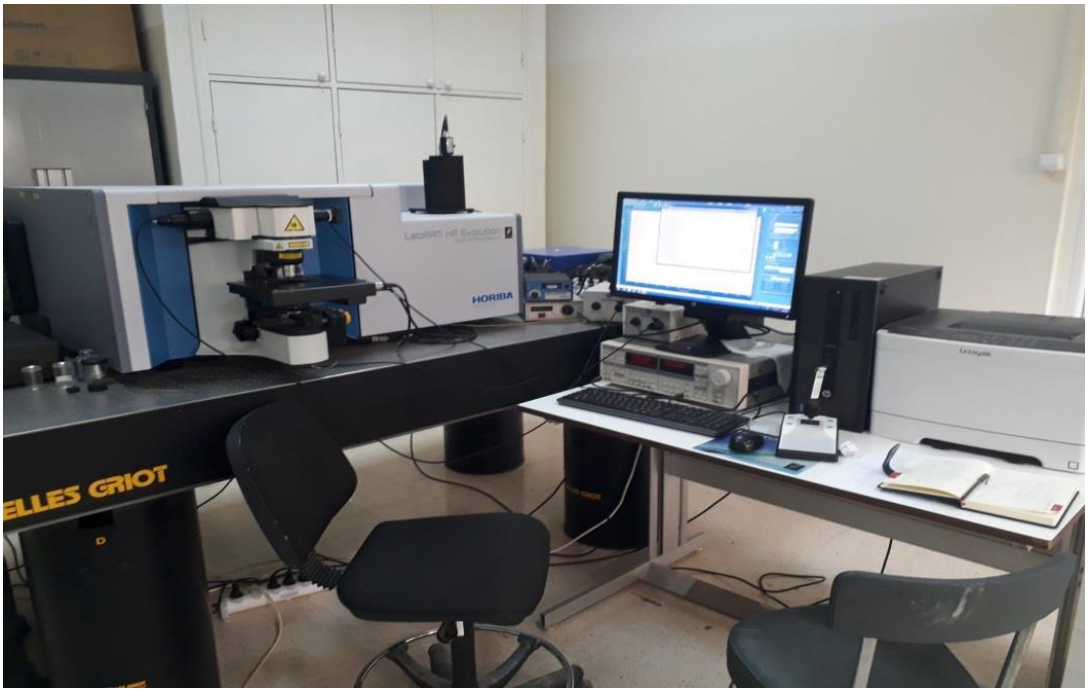

Figure III.6: *Raman spectroscopy (CDTA).*

III.5. Ultraviolet–visible–Infrared spectrophotometer

UV-VIS-IR spectroscopy is considered as the most important spectrophotometric technique. This technique works based on the measurement of the interaction of electromagnetic radiations (EMR) with the matter at a particular wavelength. The spectroscopy measures the intensity of light in UV (100–400 nm) and VIS (400–800 nm) regions as a function of wavelength. When a photon interacts with a molecule, it may induce a transition in electronic energy levels if energy provided by the photon matches with energy difference in these levels. The amount of radiations absorbed by the sample is measured and plotted against the wavelength of EMR to obtain the spectrum. Thus, a typical UV-VIS spectrum is a plot of wavelength or frequency versus the intensity of absorption. Ultraviolet-visible spectroscopy is a non-destructive technique that requires no preparation of the samples [122,123]. The spectrophotometer shown in Fig III.7 is made of a Deuterium lamp that emits a continuous spectrum in the ultraviolet region (190-400 nm) and a tungsten lamp (emitting in the 400 to 800 nm (visible)), support for the sample, a monochromator, and a detector. The operating principle of the spectrophotometer is shown in Fig III.8.

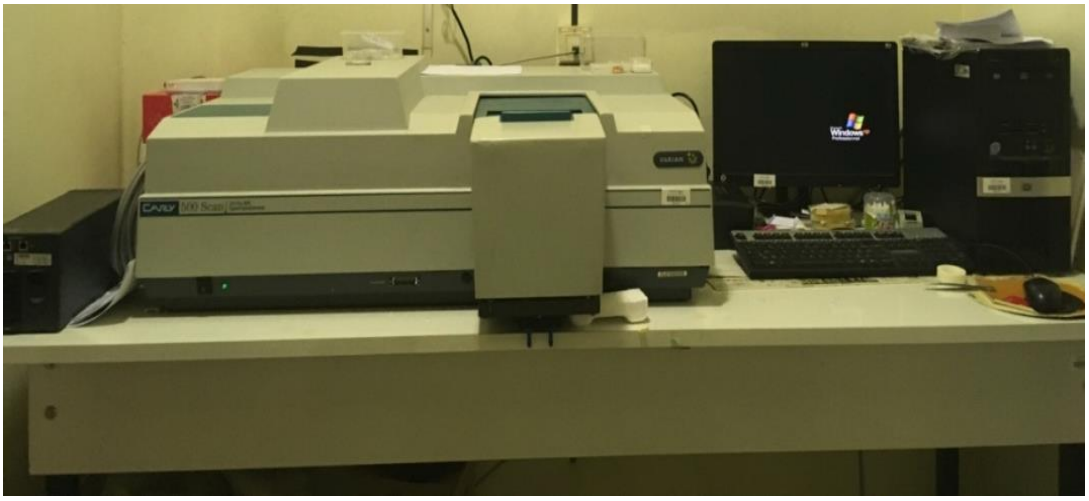

Figure III.7: *Spectrophotometer (CRTSE).*

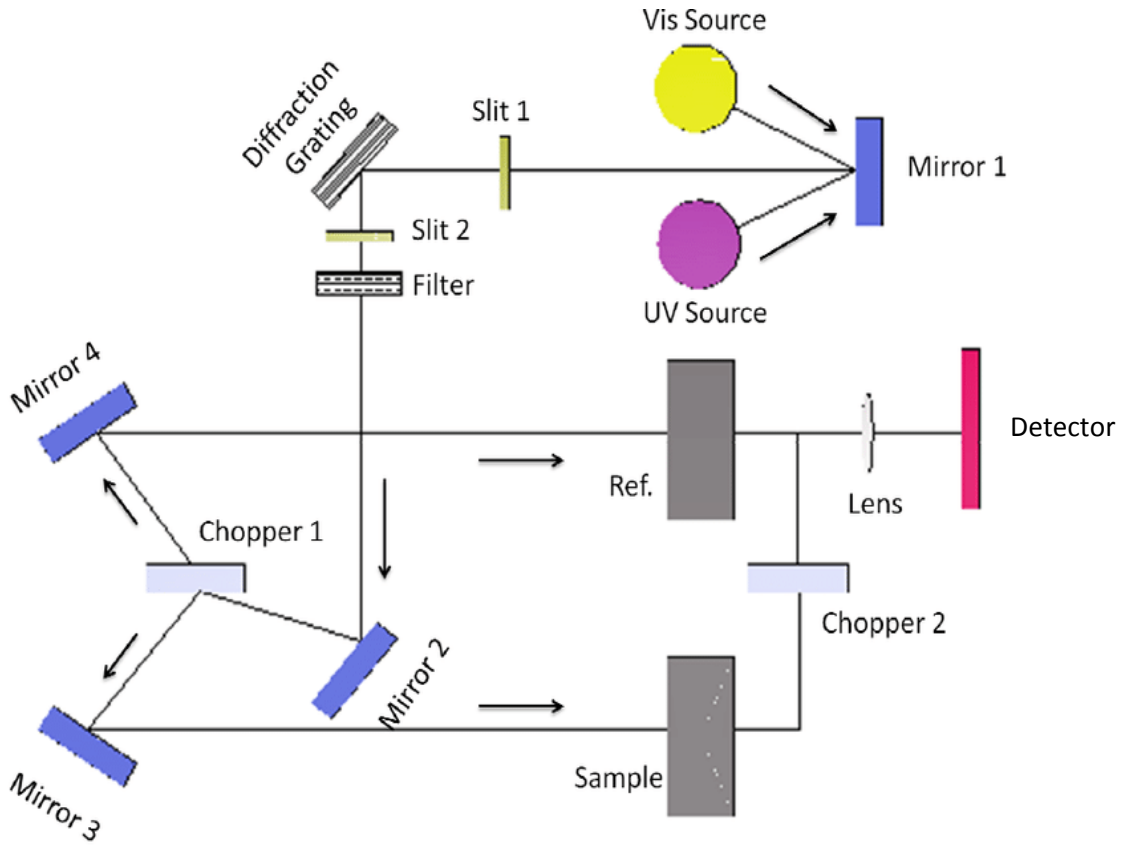

Figure III.8: *Schematic diagram of the spectrophotometer* [124].

III.6. Profilometer

This technique consists of sweeping the sample surface with a diamond-tip needle. When the tip needle locates the film substrate interface, it begins to move vertically. A linear variable differential transformer (LVDT) sensor coupled to the tip needle produces the electrical signals corresponding to the tip needle movement. These analog signals are then converted into a digital format and the software provides the thickness values [125,126].

III.7. FTIR spectroscopy

Fourier Transform Infrared Spectroscopy (FTIR) is a technique used to achieve an infrared absorption or emission spectrum of a solid, liquid, or gas. An FTIR spectrometer simultaneously collects data at a high spectral resolution over a wide energy range. It has an advantage over a dispersive spectrometer, which measures intensity over a narrow range of wavelengths at a time. The term Fourier transform infrared spectroscopy comes from the fact that a Fourier transform (a mathematical process) is required to convert raw data into the real situation of a spectrum. The objective of spectroscopy techniques (FTIR, ultraviolet-visible spectroscopy ("UV-Vis"), etc.) is to measure the amount of light absorbed by a sample at each wavelength.

The first low-cost spectrophotometer capable of recording an infrared spectrum was the Perkin-Elmer Infracord produced in 1957 [127] and has covered a wavelength range from 2.5 µm to 15 µm (wavelength range from 4000 cm-1 to 660 cm-1). The lower limit of the wavelength has been chosen to encompass the highest known vibration frequency due to a fundamental molecular vibration. Later instruments used potassium bromide prisms to extend the range to 25 µm (400 cm-1) and 50 µm (200 cm-1) for cesium iodide. Measurements required the development of precisely tuned diffraction gratings to replace prisms as scattering elements. So in the new Nicolet equipment, precisely tuned diffraction gratings have replaced prisms as scattering elements in which it can:

- ✓ Identify unknown materials
- ✓ Conduct contaminant analysis
- ✓ Reserve engineer new product
- ✓ Verify chemical structure and mixture compositions

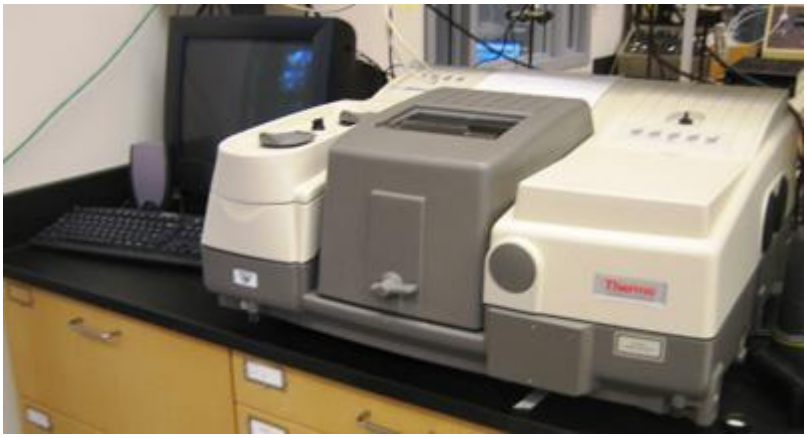

Figure III.9: *Schematic view of the FTIR spectrophotometer*

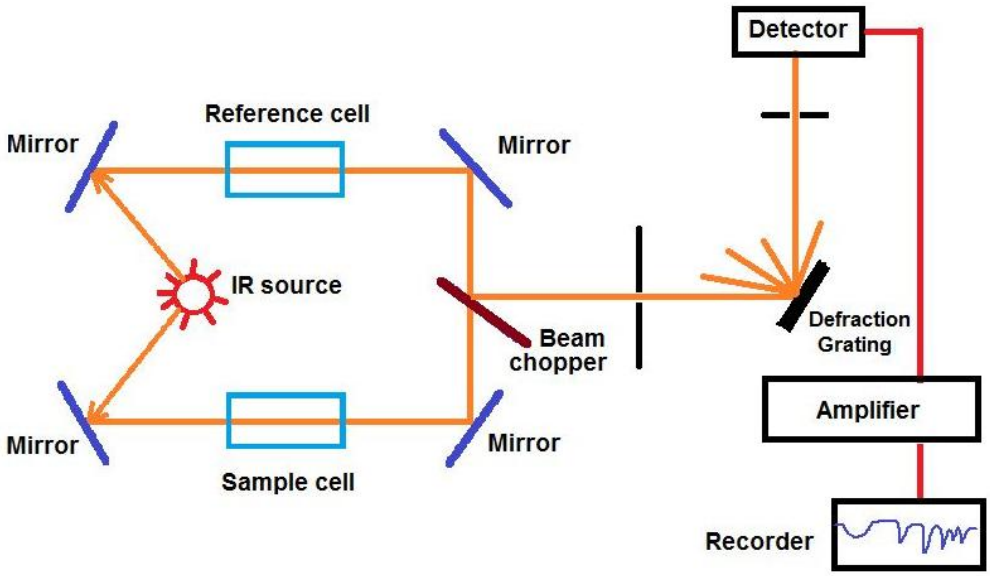

Figure III.10: *Schematic diagram of the FTIR spectrophotometer.*

III.8. Film lifetime measurement

The WCT-120 is a bench-top system for film and sample lifetime metrology, which hopes to measure the calibrated lifetime of recombination of silicon wafer, film and other carriers, using both the standard and photoluminescence methods. It is a non-destructive technique that requires no sample preparation, and is ideal for dopant diffusion and low-lifetime samples. This method complements the use of the transient photoconductance technique. The measurement of the lifetime of the quasi-stationary photoconductance

(QSSPC) also gives the implicit open circuit voltage curve (as a function of illumination), which is comparable to an I-V curve at each step of the process of a solar cell. The operating principle of the Sinton WCT-120 is shown in Figure III-11:

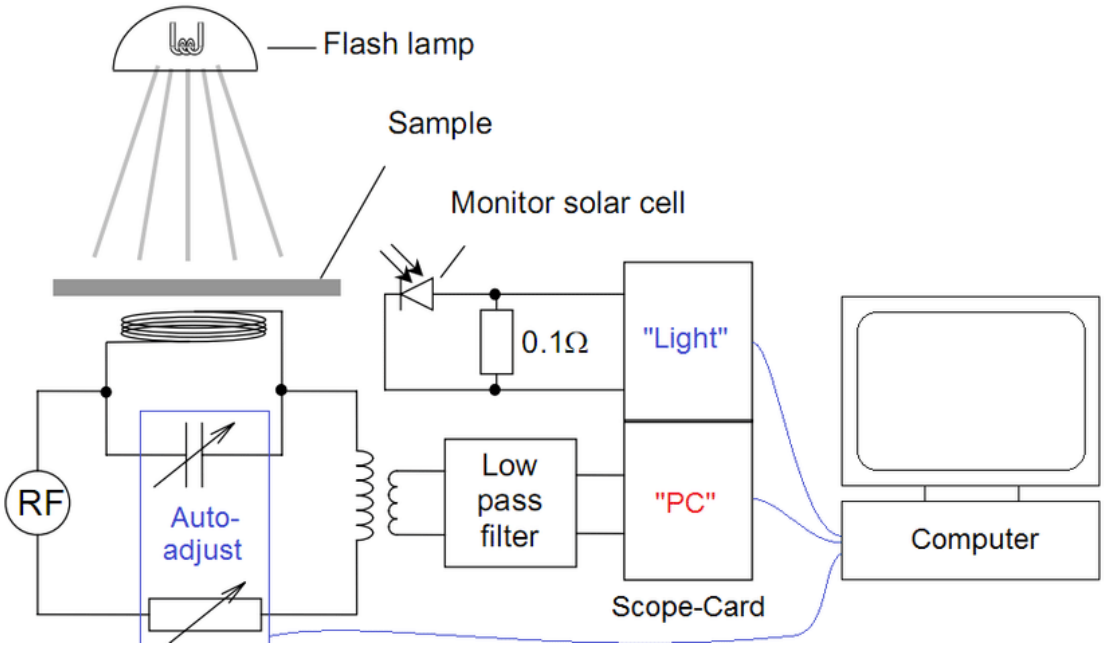

Figure III-11: *Schematics of the Sinton WCT-120 series QSSPC instrument* [128].

Figure III-12: *The WCT-120PL is an affordable, tabletop silicon lifetime and wafer metrology system.*

Chapter IV

Results and discussion

IV. Results and discussion

This last chapter is devoted to the practical study of our synthesized films regarding the structural, morphological, composition, and optical properties. However and related to the international pandemic situation, all the characterization mentioned above can't be all realized.

IV.1. Experimental details and films preparation

Iron disulfide films are depositing on (100) silicon substrate with a resistivity of 0.5-3 Ω.cm, 340µm thick, and p-type conductivity. All the samples are, first, immersing in a 4:1 concentrated H_2SO_4/H_2O_2 for 20 min at 80°C, and in a 1:1 HCl/H_2O_2 for 20 min at room temperature. Finally, the substrates are dipped in 10% HF aqueous solution at room temperature for 2 min. All the chemical processes have been completed by rinsing in the deionized water and dried in pure N_2. Then, a Chemical Bath Deposition has taken on to deposit the FeS_2 films. First, it consisted of hydrated ferrous ammonium $Fe(SO_4)_2(NH_4)_2.6H_2O$ as the cation source, thioacetamide, which is an organo-sulfur compound with the formula of C_2H_5NS, is used as the anion source, and citric acid ($C_6H_8O_7$) as the complexing agent. The complexing agent is an important component of the chemical bath because it greatly influenced the structural and electro-optical properties of the thin film. All precursors were prepared, with fixed molarities, by standard techniques. An amount of FeS cluster is added to assure the satisfaction of components needs. The pH value of the solution was adjusted to 2.5 by adding sulfuric acid H_2SO_4. The bath was maintained with a potential generator of 50 V and the solution was also vigorously stirred. The temperature is fixed to 90 °C. Then, we have prepared three samples series by varying the time deposition as 60 min, 90 min, and 120 min.

IV.2. Structural and morphology characterizations

IV.2.1 X-ray diffraction

The crystalline structure of films was investigated using the XRD technique in the 2θ scan range 30°–65°. The patterns shown in Fig.IV.1 are recorded for three samples corresponding to the 60 min, 90 min, and 120 min time deposition. The XRD measurements revealed the predominate crystallinity of the Cubic-FeS_2 phase computing h k l planes and d distance values from 2θ Bragg's angle. These values when compared with the P-phase Si_3N_4

data reported in the reference code 00-002-1366 indicate a close match within ±0.9◦ of 2θ value. The data match with those reported values in Ref. [37, 63, 83, 99].

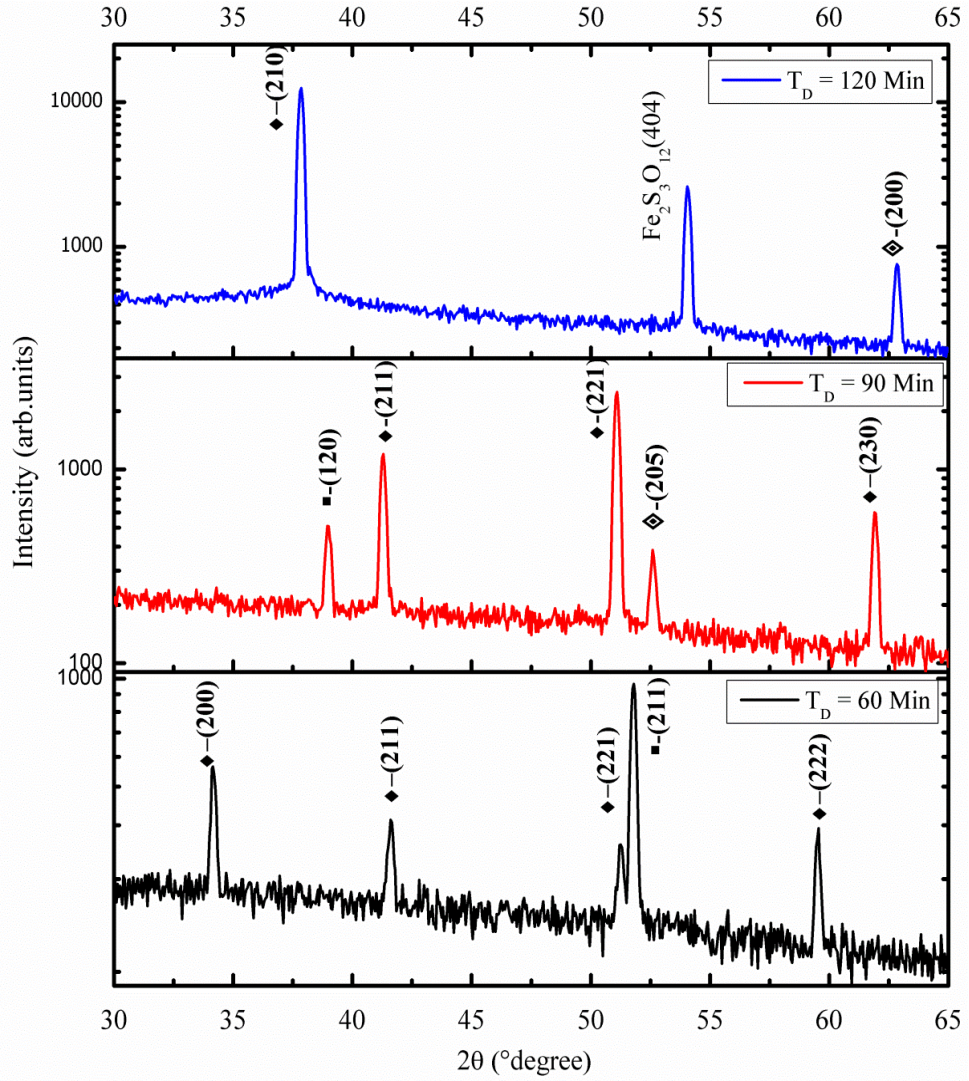

Figure IV.1: *X-ray diffraction patterns coming from three-samples corresponding to the time deposition variation.*

♦ Pyrite phase
■ Marcasite phase
◊ Troilite phase

For the first film taken at 60 min, there are peaks (200), (211), (221) and (222), which correspond to the pyrite phase and a single peak at (211) corresponds to the marcasite phase (data sheet 00-002-0908) appear with high intensity, the fact of not observing any of the chips correspond to the troilite phase. In the second sample, we notice a new peak of troilite phase in besides with peaks at (211), (221), (230) that are related to pyrite phase, and at least, one

peak (120) is corresponding to the marcasite phase , Its XRD pattern reveals that the as-prepared film consisted mainly of pyrite FeS_2 with a small amount of marcasite FeS_2.

A key point in the preparation of semiconducting pyrite is the phase purity [85, 86]. FeS_2 can crystallize not only into a cubic pyrite structure but also into an orthorhombic metastable marcasite structure.

For the last sample laying at 120 min, we notice the disappearance of peaks to marcasite phase, the survival of the peak (210) corresponds predominately to the pyrite phase. The peak (200) corresponds to the troilite and there is a one peak due to precipitation of $Fe_2S_3O_{12}$.

IV.2.2 Raman spectroscopy

As depicted in Fig.IV.2, the Raman scattering spectra, obtained from three samples, are measured as a function of the time deposition using 325 nm Ar^+ laser wavelengths (Horiba Jobin-Yvon Raman). All samples have shown slight difference. Thus, we observe a vibrational mode at 100 cm^{-1} due to bonding Fe-S, which gives evidence about the medium-range order of the crystalline lattice. As we know, the diamond structure of monocrystalline silicon (100) substrate allows only one first-order Raman active phonon, which corresponds to the transverse optic (TO) of Si at 520.5 cm^{-1}. An intense and sharp peak around the 515.5 cm^{-1} appears. The peak indicates the formation of high-quality FeS_2 nanocrystals. Based on the bond polarizability, we calculate the nanocrystals size using the analytical expression of $\Delta\omega = \chi(\delta / d)^{\gamma}$, where δ is the Si lattice parameter (0.543 nm), d is the crystalline FeS_2-NPs diameter, χ (47.41 cm^{-1}) and γ (1.44), are the model parameters. The frequency redshift was evaluated and compared with the peak at 520 cm^{-1} of pure silicon substrate that Δω=4.9 cm^{-1}, so the size of the nanocrystals is about 2.5 nm.

The broad bands located at 100, 115, 125 cm^{-1} correspond to the transversal acoustic (TA) phonon frequency of Fe-S bonds. One Raman bond located at 318 cm^{-1} are corresponding to the longitudinal acoustic (LA) of Fe-S reviling good crystallinity of iron pyrite. Moreover, the Raman band at 565 cm^{-1} is intense and reveals also good crystallinity of the C-FeS_2 and sometimes to C-C-O bonds. The peak appeared in the range 500-600 cm^{-1} show the effect of carbon impurity in the intermolecular bonds [120, 121, 124].

Also, we connected the peak at 980 cm^{-1} to the transverse optic (TO) phonons. Although all mentioned bands are assigning for the Si substrate, they were found to be dominant in Raman scattering spectra of the grown films.

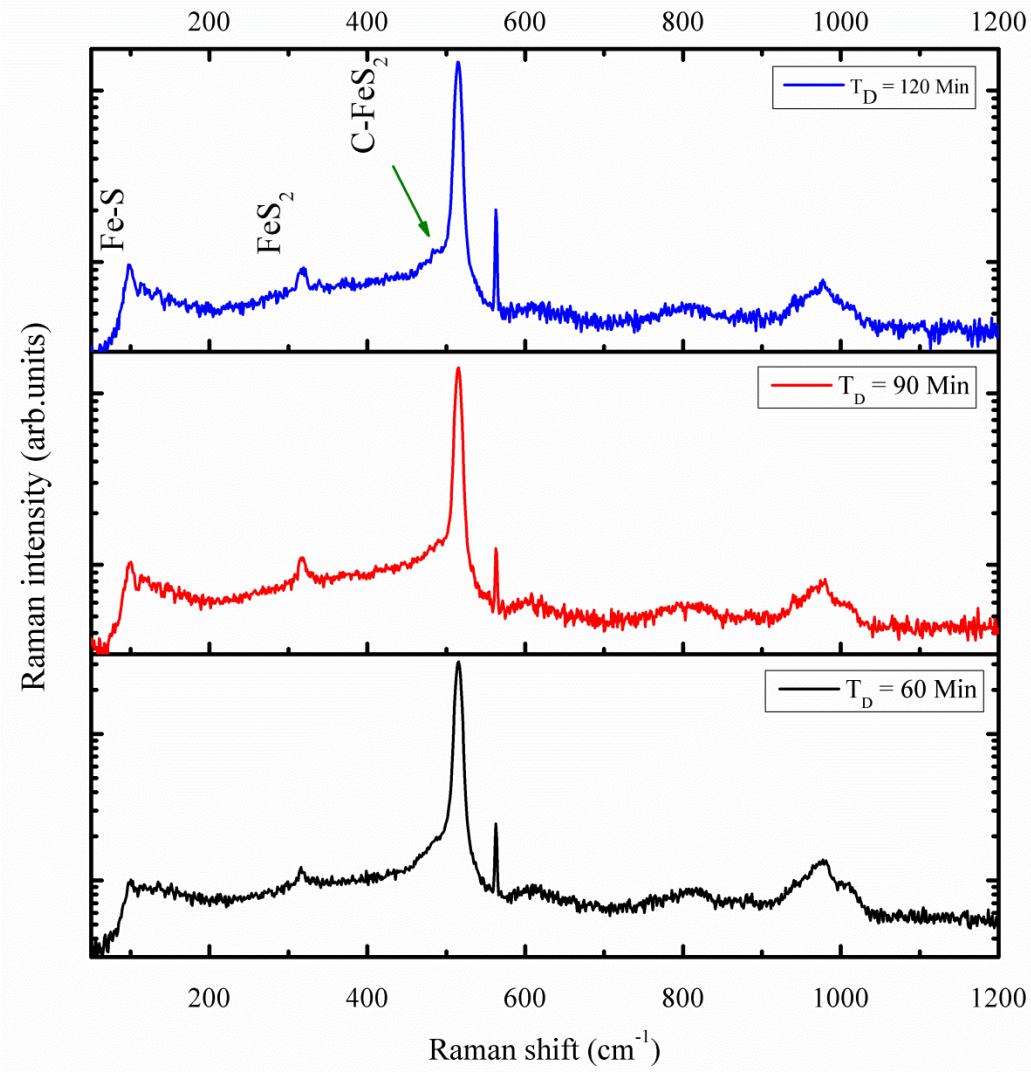

Figure IV.2: *Raman spectra in the 50–1200 cm^{-1} wavenumber range of the three samples.*

IV.2.3 SEM micrographs analysis

.As illustrated in Fig.IV.3.a-c, the resulted SEM micrographs show the evolution of the thickness and surface morphology of films linked to the time deposition of 60 min, 90 min, and 120min. The SEM micrographs in that figures show a nanometric thick pyrite films of 113, 140, and 156 nm thick, respectively. In order to further characterize the FeS_2 and no heat treatment effects on microstructural properties of the iron disulfide film, SEM analysis was carried out. In (a_2) figure, it is noted that the morphology of the surface of a thin layer of FeS_2 as-deposited is fully covered, uniform and homogeneous. In (b_2) image, we observe the beginning of the formation of small nanoparticles, which become clear and spread over the entire surface of a large size. The surface at (c_2), has a rough profile that resembles a sediment defect observed as agglomeration of fine particles [119]. Particle size and morphology cannot be clear.

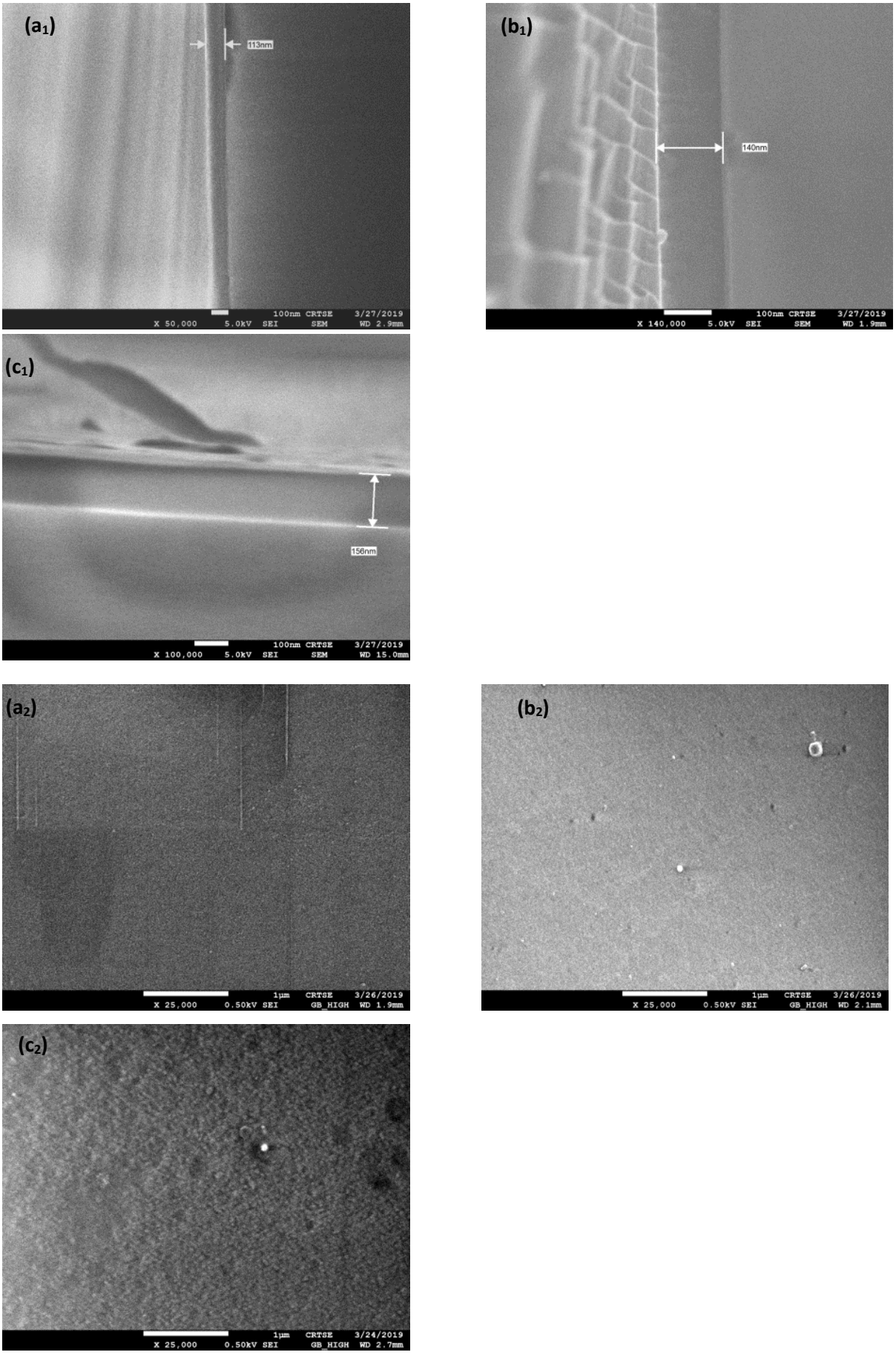

Figure IV.3: *SEM micrographs of the samples:* 60 min (a_1; a_2), 90 min (b_1; b_2), and 120 min (c_1; c_2).

IV.3. FTIR spectroscopy and composition identification

Fourier transform infrared spectroscopy (FTIR) can provide fundamental information on the molecular structure of organic and inorganic components, and is one of the most versatile analytical techniques for the non-destructive, chemical characterization of geological samples, such as coal, shale, fluid and melt inclusions, silicate glass, minerals, and microfossils, e.g., [129–130]

Figure.IV.4 has exposed the result of FTIR analyses on three samples with dominant peaks at 446 cm^{-1}, 609 cm^{-1}, and 1075 cm^{-1} corresponding to the stretching vibration absorption peaks and the bending vibration of Fe–S bond of FeS_2. Accurately, the broad absorption band of (732 cm^{-1}) and 652 cm^{-1} are, respectively, assigning to the Fe–S and Fe–Fe symmetric stretching vibrations appeared simultaneously. So the absorption band at 567 cm^{-1} corresponds to the bending vibration. On another side, the absorption band at 812 cm^{-1} is assigning to the Fe–S asymmetric stretching mode of the α-Si_3N_4 phase.

From FTIR spectrum of pyrite, Fourier-transform infrared spectra (Fig.IV.4) show various features in the 400-623 Cm^{-1} region, and broad bands around 1075 Cm^{-1}. , including modes from water and other hydroxyl-bearing species such as $Fe(OH)_3$. The band at 908, and 569 Cm^{-1} were due to stretching modes in $Fe(OH)_3$ [53, 131]. The 610 Cm^{-1}band resulted from H-O-H deformation. The shoulder bands at 515Cm^{-1} can be interpreted as respectively ν3 and ν4 frequencies of highly symmetrical SO_4^{-2} ions [36]. The bands at 446 and 423Cm^{-1} can be assigned to elemental sulfur and polysulfide species.

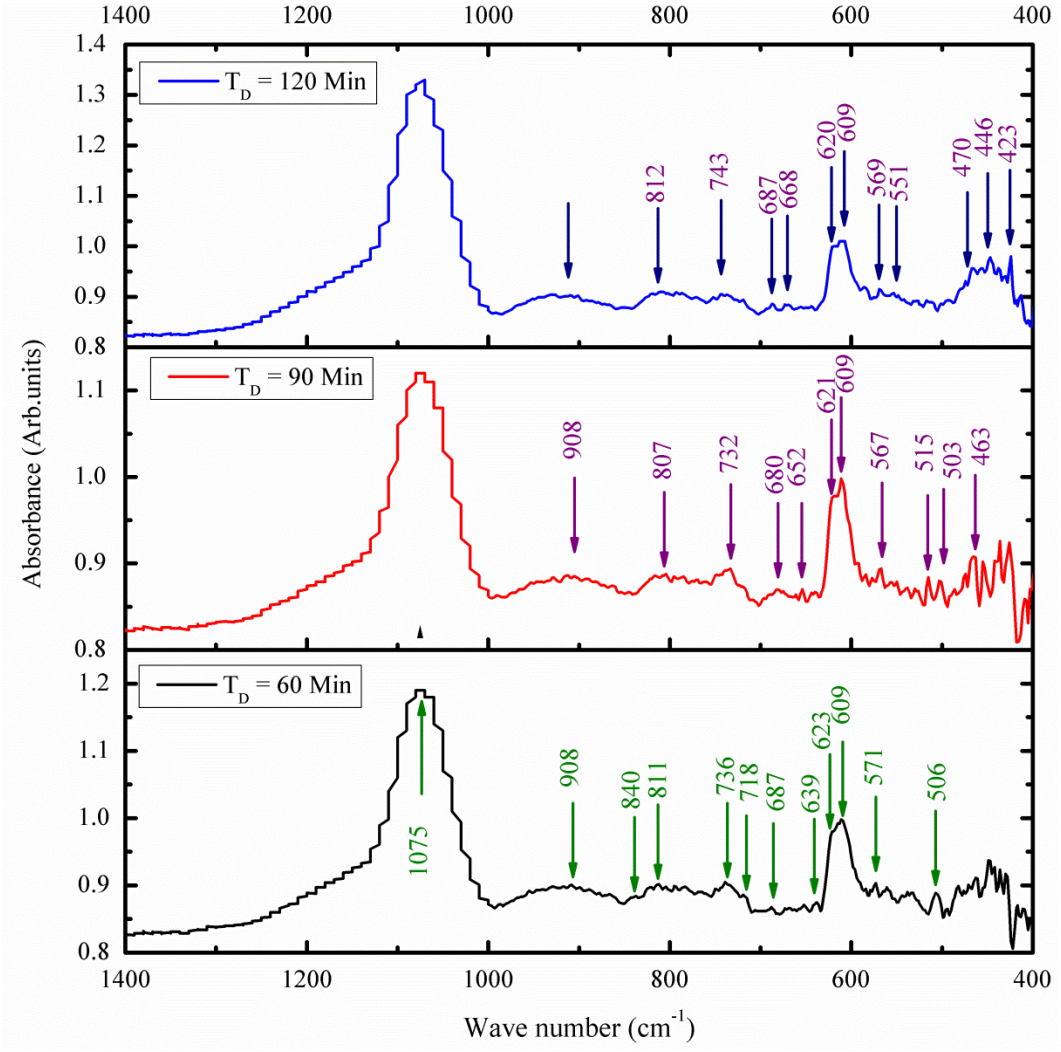

Figure IV.4: *Fourier-transform infrared (FTIR) spectra of the three samples as indicated in figure corresponding to the time deposition variation*

IV.4. Diffuse reflectance measurements

Diffuse reflection spectra are given in Fig.IV.5 focusing on the energy absorption of three samples. We have observed that these samples have a high reflection in the UV-Vis range, manifestly, at the 350 nm wavelength exhibit that the reflection peak reaches the value of ~35%. A one drop reflection is found at ~645 nm, which is attributed to the absorption threshold. It has moved down with a decrease in diffuse-reflection when the time is increased to its extinction. So, the related behavior may be due to the formation of nanostructures. The deposited film at 120 min shows specific a property of high absorption coefficient at a visible light, which is needed for photovoltaic application.

We notice roughly the same thing in the curve of 90 min; just the diffuse reflectance is less in the wavelength of 350 nm (20%), and decrease until ~1000 nm, we note that the curve is

less steep in the range 350-1000 nm. The deposition period of 60 min, have a different impact on the diffuse reflectance. It has the most value among the three curves at the wavelength 350 nm (40%) and decrease just in the range 350-115 nm, an increase in the range 115-700 nm, after that decreased in the range 700-1050 nm, after the wavelength of 1050 nm, it become almost stable. These curves show that changing the deposition period leads to a change in properties of deposited films especially the diffuse reflectance [53, 86, 99, 109, 125].

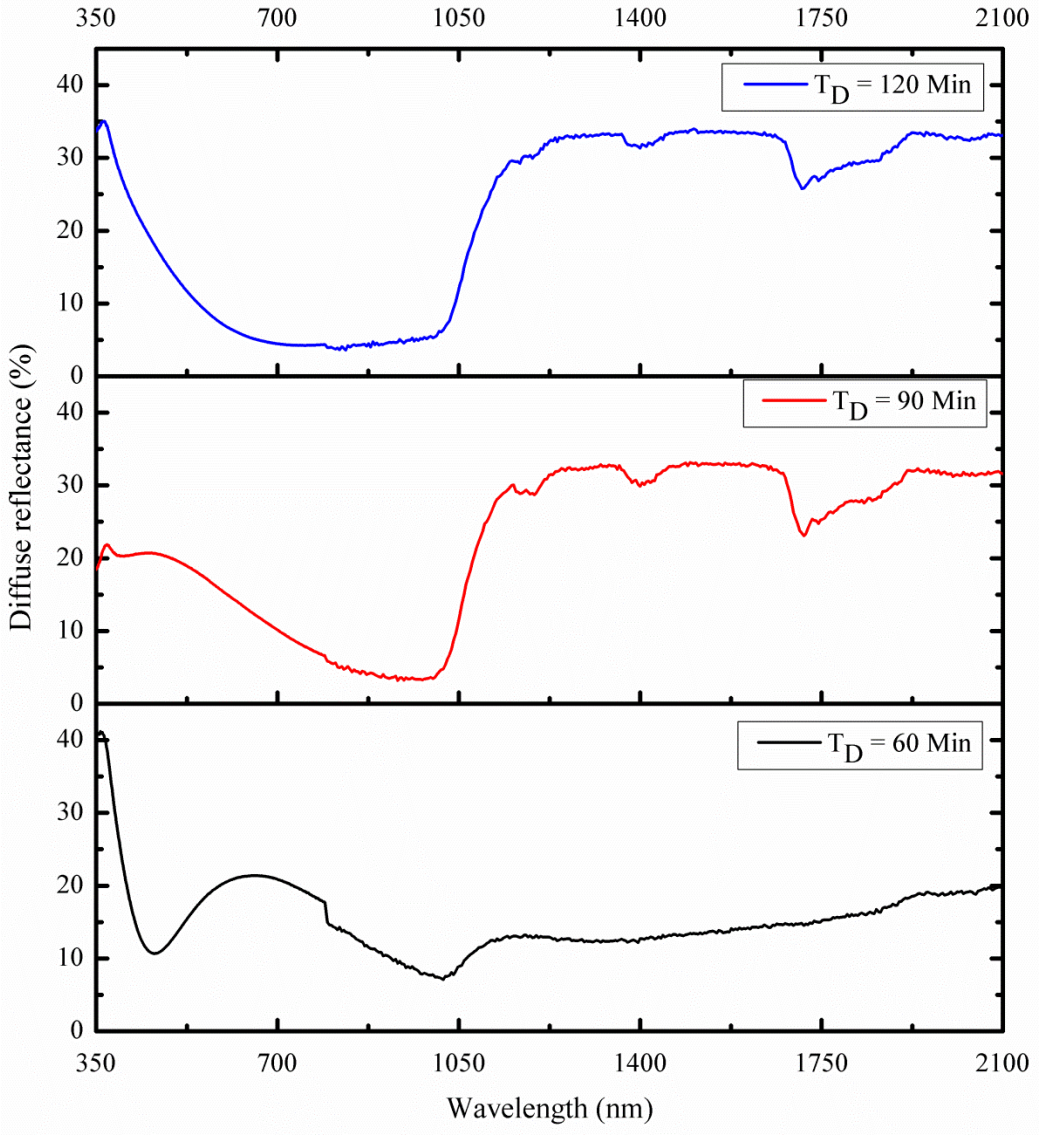

Figure IV.5: *Reflectance diffuse (%)*

According to E=hc/λ, the band gap of the host is considered to be quasi-direct and it can be expected according to:

$$\left[F(R_\infty)h\nu\right]^n = A(h\nu - E_g)$$

Where hν is the photon energy, A is a proportional constant, E_g is the value of the bandgap, n=2 for a direct transition, and $F(R_\infty)$ is the Kubelka–Munk function, which is defined as :

$$F(R_\infty) = \frac{(1-R)}{2R} = \frac{K}{S}$$

Where, R, K, and S are the diffuse reflection, the absorption and the scattering coefficient, respectively. From the linear extrapolation of $[F(R_\infty)h\nu]^2 = 0$, the E_g values were estimated.

IV.5. Lifetime results

DSSCs are promising photovoltaic devices among the third generation solar cells that have attracted considerable attention in the recent years because of their simple fabrication process, inexpensive, eco-friendliness, and high power conversion efficiency [5, 8, 34, 49, 53, 99]. A typical DSSC is comprised of three main components: A dye-absorbed TiO_2 photo-anode, a liquid electrolyte containing the I^-/I_3^- redox couple and a counter electrode (CE) [19]. Considering its important role in realizing high efficiency, one of the most important layers in DSSCs is the CE layer, which collects electrons from an external circuit and catalyzes the reduction of triiodide for regenerating the dye after electron injection [98, 134].

The C-FeS2 thin film was formed, characterized, and applied as a CE to DSSCs. The surface of the pyrite nanoparticles was coated uniformly with an amorphous carbon layer, and the pyrite nanoparticles showed high crystallinity, as illustrated by the uniform lattice spacing. Device was fabricated and we measured a device maximum power conversion efciency of~6.94% (Voc=0.6 V, and FF=89.7%). The Tafel and impedance measurements clearly show that the C-FeS_2 thin flm provided good conductivity and superior catalytic activity as the CE for DSSCs. The study demonstrated that C-FeS_2 is a promising alternative to the expensive Pt CE for future development in the low cost DSSCs.

It noticed in table the total sheet resistance differs as lifetime, because of the elaboration condition used to elaborate the samples. However, the highest lifetime was recorded for the sample C up to 6.08 µs.

Table IV.1: Details of measured lifetime in these experiments

Samples	**A_1**	**B_1**	**C_1**
Lifetime at spec.MCD (µs)	4.76	5.52	6.08
Total sheet resistance (Ohm/sq)	44.7	39.01	35.39
Measured resistivity (Ohm.cm)	1.52	1.33	1.2
Jo at 25°C (A/cm²)	1.77E-9	-1.05E-6	-
Est. Bulk Lifetime (µs)	0	0	-
Jo F it R^2	0.01	0.23	-
Lifetime at implied Vmp (µs)	112.07	-	-
Min MCD (cm^2)	-5.87E+11	-6.46E+12	-1.3E+13
Max MCD (cm^{-3})	1.17E+15	1.46E+15	1.63E+15
Bais point CD (cm^{-3})	0	0	0
Trap Density (cm^{-3})	0	0	0
Doping (cm^{-3})	7.3E+16	7.3E+16	7.3E+16
1-Sun Implied Voc (V)	0.6497	0.6104	0.621
Implied FFF (%)	89.7744	0	71.1026

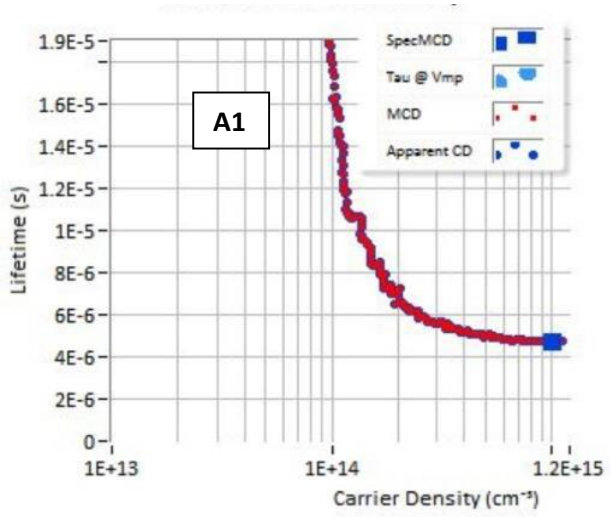

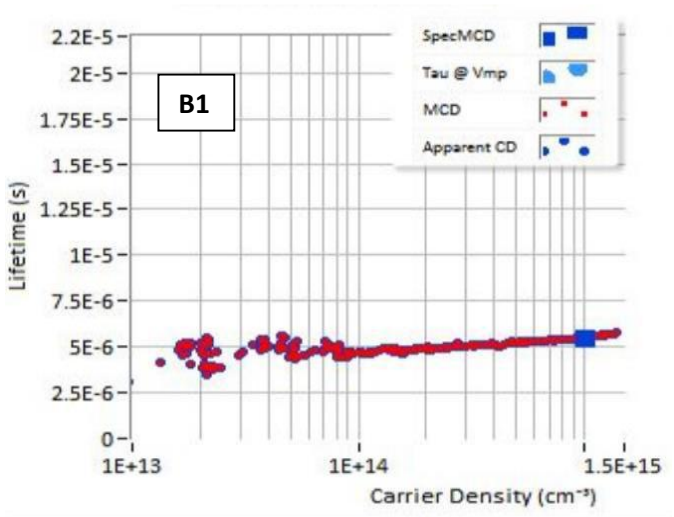

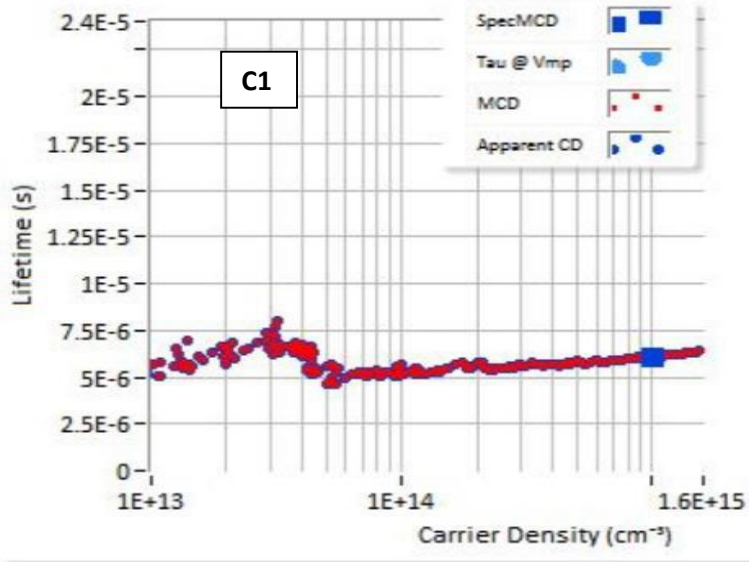

Figure IV.6: *Measurements of lifetimes of thin layer of iron disulfide*

Conclusion

Conclusion

The objective of this study is the elaboration and characterization of nanostructured iron disulfide thin films, using the possible simplest methods. Therefore, we reviewed the methods used in the literature and we noticed that the chemical vapor deposition and the chemical bath deposition are suitable for the synthesis of nanostructured iron disulfide thin films, by the use of simple and low-cost equipment, so an overview on these two methods has been done.

Chemical Bath Deposition has taken on to deposit three samples of iron disulfide thin films, with variation of deposition time. The characterization of these samples show the formation of marcasite and pyrite phases in the sample of 60 min. For this sample, the morphology of the surface is fully covered, uniform and homogeneous. And with the increase of deposition time to 90 min in the second sample, we notice that the thin film consisted mainly of pyrite with a small amount of marcasite phase, and we observe the beginning of the formation of small nanoparticles, which become clear and spread over the entire surface of a large size. The marcasite phase disappears in the 120 min sample, and the surface has a rough profile that resembles a sediment defect observed as agglomeration of fine particles. In addition, the three samples show high absorbance in the visible range.

Abundant nanostructured FeS_2, such as nanoparticles, nanowires, nanofilms, and microspherolites can be synthesized by varying experimental conditions. Nanostructured iron pyrite thin films have attracted a lot of interest in photovoltaic and photoelectrochemical applications due to their favorable electronic and optical properties. Produce of nanostructured iron pyrite thin films is an active field. Many research works have a challenge, which is the development of a simple and low-cost technique to prepare pyrite thin films with desirable morphology and properties. Developing the deposition techniques to make them more suitable and more controlibity in the preparation of thin films will lead to a great development in the field of photovoltaic and many other technologies.

References

[1] Ilan Gur, Neil A. Fromer, Michael L. Geier, A. Paul Alivisatos, Air-Stable All-Inorganic Nanocrystal Solar Cells Processed from Solution, Science 310, (2005) 462–465, https://dx.doi.org/10.1126/science.1117908.

[2] Alex Yong Sheng Eng, Jian Liang Cheong, Su Seong Lee, Controlled synthesis of transition metal disulfides ($MoS_2$and WS_2) on carbonfibers: Effects of phase and morphology toward lithium–sulfur battery performance, Appl. Mat. Today 16 (2019) 529–537, https://dx.doi.org/10.1021/nn503832j.

[3] M. Zhang, Z. Cui and H. Jiang, J. Mater. Chem. A, 2018, DOI: 10.1039/C8TA00759D.

[4] Haiying Qin, Junkang Jia, Longxia Lin, Hualiang Ni, Mudan Wang, Liang Meng, Pyrite FeS2 nanostructures: Synthesis, properties and applications, Materials Science & Engineering B 236–237 (2018) 104–124.

[5] Y. Z. Dong, Y.F. Zheng, H. Duan, Y.F. Sun, Y.H. Chen, Formation of pyrite (FeS2) thin nano-films by thermal-sulfurating electrodeposition films at different temperature, Materials Letters 59 (2005) 2398 – 2402.

[6] G. Brostigen, A. Kjekshus, Redetermined crystal structure of FeS_2 (pyrite), Acta Chem. Scand. 23 (1969) 2186–2188, http://dx.doi.org/10.3891/acta.chem.scand.23-2186.

[7] A. Ennaoui, S. Fiechter, Ch. Pettenkofer, N. Alonso-Vante, K. Buker, M. Bronold, Ch. Hopfner and H. Tributsch, "Iron disulfide for solar energy conversion," *Sol. Energ. Mat. Sol. C.* **29**, (1993) 289–370.

[8] X. Zhang, T. Scott, T. Socha, D. Nielsen, M. Manno, M. Johnson, Y. Yan, Y. Losovyj, P. Dowben, E. S. Aydil, and C. Leighton, "Phase stability and stoichiometry in thin film iron pyrite: impact on electronic transport properties," *ACS Appl. Mater. Interfaces* **7**, 14130–14139 (2015).

[9] C. Wadia, A.P. Alivisatos, D.M. Kammen, Environ. Sci. Technol. 43 (2009) 2072-2077 , https://doi.org/10.1021/es8019534

[10] T. A. Yersak, H.A. Macpherson, S.C. Kim, V.-D. Le, C.S. Kang, S.-B. Son, Y.-H. Kim, J.E. Trevey, K.H. Oh, C. Stoldt, S.-H. Lee, Adv. Energy Mater. 3 (2013) 120–127.

[11] J. Xia, J.Q. Jiao, B.L. Dai, W.D. Qiu, S.X. He, W.T. Qiu, P.K. Shen, L.P. Chen, RSC Adv. 3 (2013) 6132 http://dx.doi.org/10.1039/c6ta09060e

[12] J. Hu, Y.N. Zhang, Matt Law, R.Q. Wu, J. Ameri. Chem. Soc. 134 (2012) 13216-13219. https://dx.doi.org/10.1021/ja3053464

[13] P. Xiao, X.L. Fan, H. Zhang, X.L. Fang, L.M. Liu, J. Alloy. Comp. 629 (2015) 43-48

[14] 1. Zutic, J. Fabian, S. Das Sarma, Rev. Mod. Phys. 76 (2004) 323. https://dx.doi.org/10.1103/RevModPhys.76.323

[15] S. Bae, D. Kim, W. Lee, Appl. Catal., B 134 (2013) 93-102, https://dx.doi.org/10.1016/j.apcatb.2012.12.031

[16] M. G. Gong, A. Kirkeminde, N. Kumar, H. Zhao, S.Q. Ren, Chem. Commun. 49 (2013) 9260-9262. http://www.rsc/

[17] S. L. Liu, M.M. Li, S. Li, H.L. Li, L. Yan, Appl. Surf. Sci. 268 (2013) 213-217

[18] Yuqiao Wang, Yichao Bai, Junting Xi, Meiting Liu, Mengtian Li, Kunquan Hong, Yueming Sun, Continuous and large-area transition metal disulfides films deposited by pulsed laser/chemical vapor-combined process as a counter electrode for dye-sensitized solar cells, Materials Letters 201 (2017) 216–22.

[19] Sudhanshu Shukla, Joel W. Ager, Qihua Xiong, Thirumany Sritharan, Scientific and Technological Assesment of Iron Pyrite for Use in Solar Devices, Energy Technol. 10.1002/ente.201700638, http://dx.doi.org/10.1002/ente.201700638.

[20] Miguel Cabán-Acevedo, Matthew S. Faber, Yizheng Tan, Robert J. Hamers, and Song Jin, Synthesis and Properties of Semiconducting Iron Pyrite (FeS_2) Nanowires, dx.doi.org/10.1021/nl2045364 | Nano Lett. 2012, 12, 1977−1982.

[21] Gurpreet Kaur, Manjot Kaur, Anup Thakur, Akshay Kumar, Recent Progress on Pyrite FeS_2 Nanomaterials for Energy and Environment Applications: Synthesis, Properties and Future Prospects, Journal of Cluster Science (2019), https://doi.org.org/10.1007/s10876-019-01708-3.

[22] M. S. Jagadeesh, M. S. Seehra, Phys. Lett. A 80 (1980) https://dx.doi.org/10.1016/0375-9601(80)90454-5

[23] N. Ouarab, M. Boumaour, First-principles calculations of electronic and optical properties of $Fe_{1-x}Zn_xS_2$ and $Zn_{1-x}Mg_xO$ alloys, Curr. Appl. Phys. 17 (2017) 1169–1180 https://dx.doi.org/10.1016/j.cap.2017.05.008.

[24] W. Paszkowicz, J. A. Leiro, Rietveld refinement study of pyrite crystals, J. Alloy. Compd. 401 (1–2) (2005) 289–295, https://doi.org/10.1016/j.jallcom.2005.02.052.

[25] S. G. Choi, J. Hu, L.S. Abdallah, M. Limpinsel, Y.N. Zhang, S. Zollner, R.Q. Wu, M. Law, Pseudodielectric function and critical-point energies of iron pyrite, Phys. Rev. B 86 (2012) 115207–115211 https://doi.org/10.1103/PhysRevB.86.115207.

[26] T. Schena, G. Bihlmayer, S. Blügel, First-principles studies of FeS_2 using many-body perturbation theory in the G_0W_0 approximation, Phys. Rev. B 88 (2013) 235203–235212, https://doi.org/10.1103/PhysRevB.88.235203.

[27] V. Eyert, K.H. Höck, S. Fiechter, H. Tributsch, Electronic structure of FeS_2: the crucial role of electron-lattice interaction, Phys. Rev. B 57 (1998) 6350–6359, https://doi.org/10.1103/PhysRevB.57.6350.

[28] Y. N. Zhang, J. Hu, M. Law, R.Q. Wu, Effect of surface stoichiometry on the band gap of the pyrite FeS_2(100) surface, Phys. Rev. B 85 (2012) 085314–085318 https://doi.org/10.1103/PhysRevB.85.085314.

[29] N. Ouarab, Electronic and optical performance of Ni-doped FeS2 nanocrystals for photovoltaic applications, Physica E: Low-dimensional Systems and Nanostructures 115 (2020) 113688-1–8, https://doi.org/10.1016/j.physe.2019.113688.

[30] Nicholas Berry, Ming Cheng, Craig L. Perkins, Moritz Limpinsel, John C. Hemminger, Matt Law, Atmospheric-pressure chemical vapor deposition of iron pyrite thin films, Adv. Ener. Mater. 2 (9) (2012) 1124–1135 https://doi.org/10.1002/aenm.201200043.

[31] Leith Samad, Miguel Cabán-Acevedo, Melinda J. Shearer, Kwangsuk Park, Robert J. Hamers, Song Jin, Direct chemical vapor deposition synthesis of phase-pure iron pyrite (FeS_2) thin films, Chem. Mater. 27 (2015) 3108–3114 https://dx.doi.org/10.1021/acs.chemmater.5b00664.

[32] Kinner Tyler, Khagendra Bhandari, Ebin Bastola, M. Bradley, Neale O. Haugen Monahan, Paul J. Roland, Terry P. Bigioni, Randy J. Ellingson, Majority carrier type control of cobalt iron sulfide ($Co_xFe_{1-x}S_2$) pyrite nanocrystals, J. Phys. Chem. C 120 (2016) 5706–5713 https://dx.doi.org/10.1021/acs.jpcc.5b11204.

[33] H.S. Bennet, E.A. Stern, Faraday effect in solids, Phys. Rev. 137 (1965) A448–A461, https://doi.org/10.1103/PhysRev.137.A448.

[34] Jun Hu, Yanning Zhang, Matt Law, Ruqian Wu, First-principles studies of the electronic properties of native and substitutional anionic defects in bulk iron pyrite, Phys. Rev. B 85 (2012) 085203–085212, https://dx.doi.org/10.1103/PhysRevB.85.085203.

[35] X.-H. Wang, T. Huang, F. Huang, S.-N. Zhang, Y. Wang, C. Gao, Spectrosc. Spect. Anal. 31 (2011) 2508–2511 http://dx.doi.org/10.1021/cr300336e.

[36] J. Xia, X. Lu, W. Gao, J. Jiao, H. Feng, L. Chen, Electrochim. Acta 56 (2011) 6932-6939 https://dx.doi.org/10.1016/j.electacta.2011.06.021.

[37] N. Takahashi, Y. Nakatani, T. Yatomi, T. Nakamura, Chem. Mater. 15 (2003) 1763-1765, https://dx.doi.org/10.1021/cm0210243.

[38] L. Meng, Y.H. Liu, L. Tian, J. Cryst. Growth 253 (2003) 530–538, https://dx.doi.org/10.1016/S0022-0248(03)01040-6.

[39] C. Delasheras, I.J. Ferrer, C. Sanchez, J. Phys.-Condens. Mat. 6 (1994) 10177-10183, https://doi.org/10.1088/0953-8984/6/46/033.

[40] L. Wu, N. Y. Dzade, L. Gao, D.O. Scanlon, z. Öztürk, N. Hollingsworth, B.M. Weckhuysen, E.J. Hensen, N.H. De Leeuw, J.P. Hofmann, Adv. Mater. 28 (2016) 9602-9607, https://dx.doi.org/10.1002/adma.201602222.

[41] D. Y. Wan, B.Y. Wang, Y.T. Wang, H. Sun, R.G. Zhang, L. Wei, J. Cryst. Growth 257 (2003) 286-292, https://www.researchgate.net/deref/http%3A%2F%2Fdx.doi.org%2F10.1016%2FS0022-0248(03)01453-2

[42] B. Ouertani, J. Ouerfelli, M. Saadoun, H. Ezzaouia, B. Bessais, Thin Solid Films 516 (2008) 8584–8586, https://dx.doi.org/10.1016/j.tsf.2008.06.015.

[43] S. Huang, X. Liu, Q. Li, J. Chen, J. Alloys. Compd. 472 (2009) L9-L12, https://dx.doi.org/10.1016/j.jallcom.2010.06.051.

[44] D. Y. Wan, Y.T. Wang, B.Y. Wang, C.X. Ma, H. Sun, L. Wei, J. Cryst. Growth 253 (2003) 230-238, https://dx.doi.org/10.1179/143307511X13109310554805.

[45] Y.-H. Liu, Y. Wang, L. Meng, J. Inorg. Mater. 22 (2007) 143-147,

[46] H. Duan, Y.F. Zheng, Y.Z. Dong, X.G. Zhang, Y.F. Sun, Mater. Res. Bull. 39 (2004) 1861-1868. https://dx.doi.org/10.1016/j.materresbull.2004.06.012

[47] D. Wang, Q. Wang, T. Wang, CrystEngComm 12 (2010) 3797,

[48] J. Puthussery, S. Seefeld, N. Berry, M. Gibbs, M. Law, J. Am. Chem. Soc. 133 (2011) 716-719, https://dx.doi.org/10.1021/ja1096368

[49] Y. Bi, Y. Yuan, C.L. Exstrom, S.A. Darveau, J. Huang, Nano Lett. 11 (2011), https://dx.doi.org/10.1021/nl202902z

[50] H. A. Macpherson, C.R. Stoldt, ACS Nano 6 (2012) 8940-8949,

[51] M. Wang, C. Xing, K. Cao, L. Zhang, J. Liu, L. Meng, J. Mater. Chem. A 2 (2014) 9496-9505, http://dx.doi.org/10.1039/c5ta06458a

[52] M. Wang, D. Xue, H. Qin, L. Zhang, G. Ling, J. Liu, Y. Fang, L. Meng, Mater. Sci. Eng. B 204 (2016) 38–44,

[53] Guangmei Zhai, Rongwei Xie, Heng Wang, Jitao Zhang, Yongzhen Yang, Hua Wang, Xuemin Li, Xuguang Liu, Bingshe Xu, Effect of capping ligands on the optical properties and electronic energies of iron pyrite FeS_2 nanocrystals and solid thin films, Journal of Alloys and Compounds 674 (2016) 9-15.

[54] Ben Meester, Liesbeth Reijnen, Albert Goossens, Joop Schoonman, Synthesis of Pyrite (FeS_2) Thin Films by Low-Pressure MOCVD, Chemical Vapor Deposition 2000, 6(3), 121–128.

[55] J. R. Ares, A. Pascual, I.J. Ferrer, C.R. Sanchez, Thin Solid Films 451 (2004) 233-236.

[56] G. Baccarani, B. Ricco, G. Spadini, J. Appl. Phys. 49 (1978) 5565–5570. https://dx.doi.org/10.1063/1.324477

[57] A. L. Efros, B.I. Shklovskii, J. Phys. C 8 (1975) L49-L51, http://dx.iopscience.iop.org/0022-3719/8/11/004

[58] P. P. Altermatt, T. Kiesewetter, K. Ellmer, H. Tributsch, Sol. Energy Mater. Sol. Cells 71 (2002)181–195, https://dx.www.researchgate.net/deref/http%3A%2F%2Fdx.doi.org%2F10.1016%2FS0927-0248(01)00053-8

[59] J. Oertel, K. Ellmer, W. Bohne, J. Rohrich, H. Tributsch, J. Cryst. Growth 198 (1999) 1205-1210.

[60] E. Bastola, K.P. Bhandari, R.J. Ellingson, J. Mater. Chem. C 5 (2017) 4996-5004. https://dx.doi.org/10.1039/c7tc00948h.

[61] I. J. Ferrer, J.R. Ares, C.R. Sanchez, Sol. Energy Mater. Sol. Cells 76 (2003) 183-188, https://dx.doi.org/10.1016/S0927-0248(02)00344-6

[62] B. Koo, H. Jung, M. Park, J.-Y. Kim, H.J. Son, J. Cho, M.J. Ko, Adv. Funct. Mater. 26 (2016) 5400-5407. https://dx.doi.org/10.1002/adfm.201670156.

[63] N. Takahashi, T. Sawada, T. Nakamura, T. Nakamura, J. Mater. Chem. 10 (2000) 2346-2348 https//dx. Doi.org/10.1039/b003015p.

[64] A. K. Raturi, S. Waita, B. Aduda, T. Nyangonda, Renew. Energy 20 (2000) 37-43, https://econpapers.repec.org/scripts/redir.pf?u=https%3A%2F%2Fdoi.org%2F10.1016%252FS0960-1481%252899%252900085-3;h=repec:eee:renene:v:20:y:2000:i:1:p:37-43.

[65] K. Bilker, N. Alonso-Vante, H. Tributsch, J. Appl. Phys. 72 (1992) 5721, https://dx.doi.org/10.1063/1.351925

[66] X. Liu, J.Y.L. Ho, M. Wong, H.S. Kwok, Z.J. Liu, RSC Adv. 6 (2016) 8299-8305. https://dx.doi.org/10.1021/cm0210243.

[67] VOIGT, W. (1910). Lehrbuch der Kristallphysik. Leipzig: Teubner https//dx.doi.org/10.1007/978-3-663-15884-4

[68] SCHMID, E. & BOAS, W. (1935). Kristallplastizität. Berlin: Springer, https//dx.doi.org/10.1007/978-3-662-34532-0

[69] BHAGAVANTAM, S. & BHIMASENACHAR, J. (1946). Proc. Roy. Soc. A, 187, 381, https://dx.doi.org/10.1098/rspa.1946.0082

[70] BHIMASENACHAR, J. (1950). Proc. Nat. Inst. Sci. India, 16, 241. https://dx.doi.org/10.1007/BF03046403.

[71] BHAGAVANTAM S. & BHIMASENACHAR J. (1944). Proc. Indian Acad. Sci. 20, 298. https://dx.doi.org/10.1007/BF03046426.

[72] DORAISWAMI, M. S. (1947). Proc. Indian Acad. Sci. A, 25, 413. https://dx.doi.org/10.1007/BF03171417.

[73] SMITH, F. G. (1942). Amer. Min. 27, 1.

[74] Liuyi Huang, Feng Wang, Zhaoju Luan, Liang Meng, Pyrite (FeS2) thin films deposited by sol–gel method, Materials Letters 64 (2010) 2612–2615.

[75] Mariam Barawi, Isabel J. Ferrer, Eduardo Flores, Satoko Yoda, José R. Ares, Carlos Sánchez, Hydrogen Photoassisted Generation by Visible Light and an Earth Abundant Photocatalyst: Pyrite (FeS2), The Journal of Physical Chemistry C, 120(18), 9547–9552, doi:10.1021/acs.jpcc.5b11482.

[76] Kiyotaka Wasa, Makoto Kitabatake, Hideaki Adachi, Thin Film Materials Technology Sputtering of Compound Materials, William Andrew 2004, 17−19.

[77] S. Bausch, B. Sailer, H. Keppner, G. Willeke, E. Bucher, and G. Frommeyer, Preparation of pyrite films by plasma assisted sulfurization of thin iron films, Applied Physics Letters 57, 25 (1990); doi: 10.1063/1.104233.

[78] I. J. Ferrer, C. Sánchez, Characterization of FeS2 thin films prepared by thermal sulfidation of flash evaporated iron, Journal of Applied Physics 70, 2641 (1991); doi: 10.1063/1.349377.

[79] N. Hamdadou, A. Khelil, J.C. Bernède, Pyrite FeS2 films obtained by sulphuration of iron pre-deposited films, Materials Chemistry and Physics 78 (2003) 591–601.

[80] A. Pascual, P. Diaz-Chao, I.J. Ferrer, C. Sánchez, J.R. Ares, On the growth and doping of Fe/Ti chalcogenide thin films, Solar Energy Materials & Solar Cells 87 (2005) 575–582.

[81] B. Rezig, H. Dahman, M. Kenzari, Iron pyrite FeS2 for flexible solar cells, Renewable Energy, 2(2), 125–128. doi:10.1016/0960-1481(92)90098-n.

[82] G. Smestad, A. Da Silva, H. Tributsch, S. Fiechter, M. Kunst, N. meziani, M. Birkholz, Formation of semiconducting iron pyrite by spray pyrolysis, Solar Energy Materials 18 (1989) 299-313.

[83] A. Yamamoto, M. Nakamura, A. Seki, E.L. Li, A. Hashimoto, S. Nakamura, Pyrite (FeS2) thin films prepared by spray method using FeSO4 and (NH4)2Sx, Solar Energy Materials & Solar Cells 75 (2003) 451–456.

[84] H. Dahman, M. Khalifa, M. Brunel, B. Rezig, Iron pyrite films prepared by sulfur vapor transport, Thin Solid Films 280 (1996) 56-60.

[85] C. De las Heras, I. J. Ferrer, C. Sánchez, Comparison of pyrite thin films obtained from Fe and natural pyrite powder, Applied Surface Science 50 (1991) 505-509.

[86] C. De las Heras, I.J. Ferrer, C. Sánchez, Temperature dependence of the optical absorption edge of pyrite FeS_2 thin films, Journal of Physics: Condensed Matter, 6(46), 10177–10183, doi:10.1088/0953-8984/6/46/033.

[87] Qi Zhang, Daniel Sando, Valanoor Nagarajan, Chemical route derived bismuth ferrite thin films and nanomaterials, Journal of Materials Chemistry C, 4(19), 4092–4124, doi:10.1039/c6tc00243a.

[88] K. Anuar, W.T. Tan, Md. Jelas, S.M. Ho, S.Y. Gwee, Effects of Deposition Period on the Properties of FeS_2 Thin Films by Chemical Bath Deposition Method, Science & Technology Asia(2010), 15(2), 62-69.

[89] Avinash S. Dive, Ketan P. Gattu, Nanasaheb P. Huse, Devesh R. Upadhayay, D.M. Phase, Ramphal B. Sharma, Single step chemical growth of ZnMgS nanorod thin film and its DFT study, Materials Science & Engineering B 228 (2018) 91–95.

[90] Kaiwen Sun, Zhenghua Su, Jia Yang, Zili Han, Fangyang Liu, Yanqing Lai, Jie Li, Yexiang Liu, Fabrication of pyrite FeS2 thin films by sulfurizing oxide precursor films deposited via successive ionic layer adsorption and reaction method, Thin Solid Films 542 (2013) 123–128.

[91] S. Seefeld, M. Limpinsel, Y. Liu, N. Farhi, A. Weber, Y.N. Zhang, N. Berry, Y.J. Kwon, C.L. Perkins, J.C. Hemminger, R.Q. Wu, M. Law, Iron Pyrite Thin Films Synthesized from an Fe(acac)3 Ink, J. Am. Chem. Soc. 135 (2013) 4412–4424.

[92] Soumitra Kar, Subhadra Chaudhuri, Solvothermal synthesis of nanocrystalline FeS2 with different morphologies, Chemical Physics Letters 398 (2004) 22–26.

[93] A. Kirkeminde, B.A. Ruzicka, R. Wang, S. Puna, H. Zhao, S. Ren, Synthesis and Optoelectronic Properties of Two-Dimensional FeS_2 Nanoplates, A.C.S. Appl. Mater. Interfaces 4 (2012) 1174–1177.

[94] Y. Hu, Z. Zheng, H. Jia, Y. Tang, L. Zhang, Selective Synthesis of FeS and FeS2 Nanosheet Films on Iron Substrates as Novel Photocathodes for Tandem Dye-Sensitized Solar Cells, J. Phys. Chem. C 112 (2008) 13037–13042.

[95] M.-L. Li, Q.-Z. Yao, G.-T. Zhou, X.-F. Qu, C.-F. Mu, S.-Q. Fu, Microwave-assisted controlled synthesis of monodisperse pyrite Microspherolites, CrystEngComm 13 (2011) 5936.

[96] Jan-Otto Carlsson and Peter M. Martin, Handbook of Deposition Technologies for Films and Coatings (Third Edition), Science, Applications and Technology (2010), Pages 314-363, https://doi.org/10.1016/B978-0-8155-2031-3.00007-7.

[97] D. M. Schleich and H. S. W. Chang, Iron pyrite and iron marcasite thin films prepared by low pressure chemical vapor deposition, Journal of Crystal Growth 112 (1991) 737—744.

[98] B. Thomas, C. Hopfner, K. Ellmer, S. Fiechter, H. Tributsch, Growth of FeS_2 (pyrite) thin films on single crystalline substrates by low pressure metalorganic chemical vapour deposition, Journal of Crystal Growth 146 (1995) 630-635.

[99] Naoyuki Takahashi, Takuma Yatomi, Takato Nakamura, Crystal quality, electrical and optical properties of single crystal pyrite films prepared by chemical vapor deposition under atmospheric pressure, Solid State Sciences 6 (2004) 1269–1272.

[100] S. K. Bhar, S. Jana, A. Mondal, and N. Mukherjee (2013). J. Colloid Interface Sci. 393, 286.

[101] A. Baruth, M. Manno, D. Narasimhan, A. Shankar, X. Zhang, M. Johnson, E. S. Aydil, and C. Leighton (2012). J. Appl. Phys. 112, 054328-13.

[102] Anthony C. Jones, Michael L. Hitchman, Chemical Vapour Deposition Precursors, Processes and Applications, Royal Society of Chemistry (2009), 5-6.

[103] Aida, M. S., & Hariech, S. (2020). Cadmium Sulfide Thin Films by Chemical Bath Deposition Technique. Advances in Material Research and Technology, 49–75. doi:10.1007/978-3-030-50108-2_3.

[104] Schneller, T., Waser, R., Kosec, M., & Payne, D. (Eds.). (2013). Chemical Solution Deposition of Functional Oxide Thin Films. doi:10.1007/978-3-211-99311-8.

[105] Hodes, G. (2007). Semiconductor and ceramic nanoparticle films deposited by chemical bath deposition. Physical Chemistry Chemical Physics, 9(18), 2181. doi:10.1039/b616684a.

[106] Nair, P. (1998). Semiconductor thin films by chemical bath deposition for solar energy related applications. Solar Energy Materials and Solar Cells, 52(3-4), 313–344. doi:10.1016/s0927-0248(97)00237-7.

[107] Vedavathi Aluri, Kotte Thulasi Ramakrishna Reddy, Yerpedu Munikrishna Reddy, Polycrystalline and single phase FeS_2 films grown by chemical bath deposition, Nanotechnol Rev 2015; 4(5): 469–472.

[108] K. Anuar, W.T. Tan, N. Saravanan, S.M. Ho, S.Y. Gwee, Influence of pH Values on Chemical Bath Deposited FeS_2 Thin Films, The Pacific Journal of Science and Technology, Vol 10, N° 2 (2009).

[109] Qikai Yu, Shu Cai, Zhengguo Jin, Zipeng Yan, Evolutions of composition, microstructure and optical properties of Mn-doped pyrite (FeS_2) films prepared by chemical bath deposition, Materials Research Bulletin 48 (2013) 3601–3606.

[110] Tian, Z. R., Voigt, J. A., Liu, J., Mckenzie, B., Mcdermott, M. J., Rodriguez, M. A., … Xu, H. (2003). Complex and oriented ZnO nanostructures. Nature Materials, 2(12), 821–826. doi:10.1038/nmat1014.

[111]Junko Yahiro, Tetsuo Kawano, Hiroaki Imai, Nanometric morphological variation of zinc oxide crystals using organic molecules with carboxy and sulfonic groups, Journal of Colloid and Interface Science 310 (2007) 302–311.

[112]Abraham Ulman, Formation and Structure of Self-Assembled Monolayers, Chem. Rev. 1996, 96, 1533-1554.

[113]J. Sagiv, Organized monolayers by adsorption. 1. Formation and structure of oleophobic mixed monolayers on solid surfaces. Journal of the American Chemical Society, 102(1) (1980) 92–98. doi:10.1021/ja00521a016.

[114]George M. Whitesides, Self-Assembling Materials, Scientific American, Vol. 273, No. 3 (1995), pp. 146-149.

[115]A.R. Bushroa, R.G. Rahbari, H.H. Masjuki, M.R. Muhamad, Approximation of crystallite size and microstrain via XRD line broadening analysis in TiSiN thin films, Vacuum 86 (2012) 1107e1112.

[116]J. Epp, X-ray diffraction (XRD) techniques for materials characterization. Materials Characterization Using Non-destructive Evaluation (NDE) Methods, (2016) 81–124. doi:10.1016/b978-0-08-100040-3.00004-3.

[117]De Assumpção Pereira-da-Silva, M., & Ferri, F. A. (2017). Scanning Electron Microscopy. Nanocharacterization Techniques, 1–35. doi:10.1016/b978-0-323-49778-7.00001-1.

[118]Semnani, D. (2017). Geometrical characterization of electrospun nanofibers. Electrospun Nanofibers, 151–180. doi:10.1016/b978-0-08-100907-9.00007-6.

[119]Henning, S., & Adhikari, R. (2017). Scanning Electron Microscopy, ESEM, and X-ray Microanalysis. Microscopy Methods in Nanomaterials Characterization, 1–30. doi:10.1016/b978-0-323-46141-2.00001-8.

[120]Bumbrah, G. S., & Sharma, R. M. (2016). Raman spectroscopy – Basic principle, instrumentation and selected applications for the characterization of drugs of abuse. Egyptian Journal of Forensic Sciences, 6(3), 209–215. doi:10.1016/j.ejfs.2015.06.001.

[121]John, N., & George, S. (2017). Raman Spectroscopy. Spectroscopic Methods for Nanomaterials Characterization, 95–127. doi:10.1016/b978-0-323-46140-5.00005-4.

[122]Akash, M. S. H., & Rehman, K. (2020). Essentials of Pharmaceutical Analysis. doi:10.1007/978-981-15-1547-7.

[123]Shard, A. G., Schofield, R. C., & Minelli, C. (2020). Ultraviolet–visible spectrophotometry. Characterization of Nanoparticles, 185–196. doi:10.1016/b978-0-12-814182-3.00012-2.

[124]Kafle, B. P. (2020). Theory and instrumentation of absorption spectroscopy. Chemical Analysis and Material Characterization by Spectrophotometry, 17–38. doi:10.1016/b978-0-12-814866-2.00002-6.

[125]J. M. Bennett, L. Mattsson, Introduction to Surface Roughness and Scattering, Optical Society of America, Washington, D.C.

[126]K. J. Stout and L. Blunt, Three-Dimensional Surface Topography Second Edition (2000).

[127]The Infracord double-beam spectrophotometer". Clinical Science. 16 (2). 1957.

[128]M D Abbott, J E Cotter, F W Chen, and T Trupke, "Application of photoluminescence characterization to the development and manufacturing of highefficiency silicon solar cells.," *J. App. Phy.*, vol. 100, pp. 114514-114514-10, December 2006.

[129]W. Yumiko, F. James, O. Hiroshi, Anomalous fractionations of sulfur isotopes during thermochemical sulfate reduction, Science 324 (2009) 370e373

[130]C. Gil-Lozano, A.F. Davila, E. Losa-Adams, A.G. Fairen, L. Gago-Duport, Quan- tifying Fenton reaction pathways driven by self-generated H2O2 on pyrite surfaces, Sci. Rep. 7 (2017) 43703e43710

[131]D.P. Tao, P.E. Richardson, G.H. Luttrell, R.H. Yoon, Electrochemical studies of pyrite oxidation and reduction using freshly-fractured electrodes and rotating ring-disc electrodes, Electrochim. Acta 48 (24) (2003) 3615e3623.

[132]S. Thomas, T.G. Deepak, G.S. Anjusree, T.A. Arun, S.V. Nair, A.S. Nair, A review on counter electrode materials in dye-sensitized solar cells. J. Mater. Chem. A2, 4474–4490 (2014).